AIAA SciTech
4-8 January 2016, San Diego, California, USA
AIAA Atmospheric Flight Mechanics Conference

The Dynamics of Passive Wing-Pitching in Hovering Flight of Flapping Micro Air Vehicles Using Three-Dimensional Aerodynamic Simulations

Longlong Chang*, Néstor O. Pérez-Arancibia†

University of Southern California, Los Angeles, CA 90089, USA

We present a study of the dynamics of passive wing-pitching in flapping hovering flight, employing a computational simulation approach. Here, we describe the motion of a perfectly rigid wing using Lagrangian dynamics, where the external generalized moment acting on the system is the total aerodynamic moment produced by the interaction of the moving wing with the air. The passive rotating mechanism (hinge) is modeled using elastic beam theory and the total aerodynamic moment is computed by numerically solving the three-dimensional Navier-Stokes equations for the low Reynolds number case, using an overset grid method. The proposed approach leads to the formulation of a fluid-structure interaction problem, which is solved using an alternating time marching procedure, where the solution to the rigid-body dynamics of the wing at time t_{n+1} is updated using the total aerodynamic moment computed at time t_n. Then, the updated rigid-body wing dynamics information is used to find the boundary conditions required to solve the Navier-Stokes equations at time t_{n+1}, allowing one to update the aerodynamic moment required to continue with the procedure. The proposed method for simulating the fluid-structure interaction phenomenon is validated using experimental data available in the technical literature. Future generalizations of the method discussed here have the potential to significantly impact the way flapping-wing *micro air vehicles* (MAVs) are designed and controlled.

NOMENCLATURE

$\mathbb{F}_0$, $\mathbb{F}_\mathrm{b}$	=	inertial frame, wing-fixed (body) frame
$\mathbf{e_X}$,$\mathbf{e_Y}$,$\mathbf{e_Z}$	=	unit vectors associated with the inertial frame $\mathbb{F}_0$, corresponding to axes $\mathbf{X}, \mathbf{Y}, \mathbf{Z}$
$\mathbf{e_x}$, $\mathbf{e_y}$, $\mathbf{e_z}$	=	unit vectors associated with the body frame $\mathbb{F}_\mathrm{b}$, corresponding to axes $\mathbf{x}, \mathbf{y}, \mathbf{z}$
ϕ, θ, ψ	=	Euler angles associated with the flapping, pitching and rolling rotations
E, κ	=	Young's modulus of the hinge material, curvature of the deformed hinge
I_h	=	second moment of area of the hinge cross section
k_h, M_h	=	torsional stiffness coefficient of the hinge, external moment applied to the hinge
l_h, w_h, τ_h, h_o	=	length, width and thickness of the hinge, position of the wing-pitching axis
L, K, V	=	Lagrangian, kinetic energy, potential energy
q, $\dot{q}$	=	generic generalized coordinate, generic generalized velocity
$\mathbf{F}_i$, $\mathbf{M}_i$	=	external force and moment on the center of mass of the ith linkage-component
$\mathbf{v}_i$, $\boldsymbol{\omega}_i$	=	velocity of the center of mass, angular velocity of the ith linkage-component
$\mathrm{J_b}$	=	wing's moment of inertia matrix with respect to $\mathbb{F}_\mathrm{b}$
J_x, J_y, J_z	=	wing's moment of inertia components with respect to $\mathbb{F}_\mathrm{b}$
J_{xy}, J_{yz}, J_{zx}	=	wing's product of inertia components with respect to $\mathbb{F}_\mathrm{b}$
$\mathbf{v}_\mathrm{c}$, $\boldsymbol{\omega}$	=	velocity of the wing's center of mass, angular velocity of the wing
$\mathbf{F}_\mathrm{c}$, $\mathbf{M}_\mathrm{c}$	=	external force and moment on the wing's center of mass
$\mathbf{M}_\mathrm{ae}$	=	aerodynamic moment applied to the wing about the inertial origin
$M_{\mathrm{ae},\mathbf{x}}$, $M_{\mathrm{ae},\mathbf{y}}$, $M_{\mathrm{ae},\mathbf{z}}$	=	aerodynamic moment components with respect to $\mathbb{F}_\mathrm{b}$

*PhD. Student, Department of Aerospace and Mechanical Engineering, Viterbi School of Engineering, AIAA Member.
†Assistant Professor, Department of Aerospace and Mechanical Engineering, Viterbi School of Engineering.

$\tilde{M}_\theta$, $\tilde{M}_\phi$	=	generalized moments along θ, ϕ directions
ρ, ν	=	air density, kinematic viscosity of air
$\mathbf{u}$, p	=	velocity of the air flow field, pressure of the air flow field
$\mathbf{f}_{\mathrm{pres},i}$, $\mathbf{f}_{\mathrm{shear},i}$	=	pressure force, viscous shear force on the ith wing-surface element
$\mathbf{a}_i$, $\mathbf{T}_i$	=	vector area element, shear-stress tensor of the ith wing-surface element
$F_{\mathrm{ae},\mathbf{l}}$, $M_{\mathrm{ae},\mathbf{l}}$	=	aerodynamic force, aerodynamic moment, along the generic direction $\mathbf{l}$
$\mathbf{F}_\mathrm{p}$, $\mathbf{M}_\mathrm{p}$	=	pressure force, pressure moment, acting on the wing surface
x_cp, y_cp, z_cp	=	location of the wing's center of pressure with respect to $\mathbb{F}_\mathrm{b}$
ζ^{-1}	=	unit delay operator
μ	=	auxiliary variable for the solution of *ordinary differential equations* (ODEs)
Π_ae, G, g	=	auxiliary functions in iteration formulas for the solution of ODEs
P_sys	=	total instantaneous power consumption in the flapping-wing system
P_ae, P_in	=	aerodynamic power and inertial power in the flapping-wing system
P_hg, P_diss	=	hinge power, power dissipated as sound and heat by the moving wing
F_Z, F_L	=	total generated vertical force, total vertical aerodynamic force (lift)
Z_c, a_Z	=	vertical position and acceleration of the wing's center of mass with respect to $\mathbb{F}_0$
R, $\bar{c}$, c_max	=	spanwise length, standard mean chord, and maximum chord of the wing

I. INTRODUCTION

The development of micro-mechanisms based on the notion of passive wing-pitching made possible the design and fabrication of insect-scale flapping-wing *micro air vehicles* (MAVs)[1]. For example, in Ref. 1, the wings of the MAV are actively flapped, but wing-pitching is achieved passively as the MAV's wings rotate about flexure hinges, a result of the wing's interaction with the surrounding air and the influence of inertial forces. Recently, the introduction of new fabrication methods[2,3] and control techniques[4,5,6,7] have enabled the creation of increasingly more sophisticated and maneuverable flying microrobots, with weights ranging from ≈ 70 mg to ≈ 120 mg[8,9,10,11]. Similarly, passive wing rotation has been demonstrated to be effective in the creation of small-bird-scale flapping-wing machines[12,13]. These numerous successful experimental cases have sparked the curiosity of researchers in multiple directions. For example, in Ref. 14, a shape-memory-polymer-based method is proposed to actively change the stiffness of the passively rotating mechanism of a flapping wing. In Ref. 15, a quasi-steady blade-element method is used to analyze flapping-wing experimental data and provide a better understanding on the generation of aerodynamic forces by passive rotation in flapping-wing flight. In the research presented in Ref. 16, a *two-dimensional* (2-D) Navier-Stokes numerical solver, based on the discontinuous Galerkin method, was developed and employed to compute the instantaneous lift and drag forces acting on a flapping-and-rotating wing, using prescribed flapping and wing-pitching kinematic trajectories, which were obtained from a previous experiment.

The results published in both papers, Refs. 15 and 16, represent a significant step toward the understanding of aerodynamic force generation in passively-rotating flapping wings. However, the systematic development of novel aerodynamic designs and the synthesis of new robust control methods for autonomous flapping-wing flight require a more sophisticated description of the fluid-structure interaction phenomena that generate the forces necessary for flight. A specific topic that deserves further research is the generation of instantaneous aerodynamic forces acting distributedly on MAVs' wing surfaces. Considering the high complexity of the experiments required to measure force distributions on flapping wings, it results natural to pursue a simulation-based approach, using existing *computational fluid dynamics* (CFD) tools. In cases where both the flapping and pitching motions of the wings are actively generated, numerical simulations can be implemented using fully prescribed wing kinematics. In the case considered here, where flapping motions are generated actively but wing-pitching motions are generated passively with the use of a flexure hinge (torsional spring), a fluid-structure interaction problem arises. The wings of interest here[1], made of polymer membranes and reinforced with carbon fiber structures, can be modeled as rigid thin plates, rotating about hinge centerlines (pitching), which generally define second-order nonlinear oscillatory problems. Notice that in this formulation, the flexure hinge produces a restoring moment[15] and the aerodynamic forces generate a damping moment.

In the proposed simulation scheme, the flapping motion is fully prescribed, as it models the direct action of a controlled power actuator, and the wing-pitching motion is described by a rotational dynamic differential equation, where the external excitation is the instantaneous aerodynamic force distribution generated by the interaction of the flapping wing with the surrounding air. Under this paradigm, the wing dynamical behavior is essentially determined by the characteristics of the restoring moment exerted by the flexure hinge. In the linear elastic case, the restoring moment is proportional to the wing-pitching angle, where the proportional stiffness coefficient can be estimated using simple single-axis bending beam theory[17,15,18]. If the flexure hinge is nonlinear or tunable (time-varying), its mechanical behavior can be simulated using experimentally collected data (arranged in look-up tables) and interpolation, or methods based on *finite element analysis* (FEA)[19,14]. In most of the recent literature on passive rotation, linear models of torsional stiffness are used in analysis and simulations[15]. This is the same approach we follow in the simulations discussed here, considered to be a first the generation of results. However, it is uncertain if the assumption of a linear restoring moment, which follows from simple bending theory, actually holds for large wing-pitching angles, and therefore, this issue deserves further scrutiny and validation, which can be accomplished through the use of integrated simulations and/or experiments.

Here, once the flexure hinge has been modeled and the dynamic equations describing the motion of the wing have been formulated, what remains is the computation, in every time step, of the instantaneous aerodynamic forces acting on the wing's surfaces, generated by the interaction of the wing with the surrounding air, as it flaps actively and pitches passively over a flapping cycle. As a modeling tool and simulation strategy, the distributed aerodynamic forces are computed at each simulation step by numerically solving a Navier-Stokes problem. From the *partial differential equations* (PDEs) perspective, a wing (actively flapping and passively pitching) with a time-varying attitude in space defines moving boundary conditions, which represents the major challenge to overcome in the numerical simulation of the dynamics discussed in this paper[20]. Specifically, a moving boundary condition significantly increases the complexity of a CFD simulation compared to a problem with a static boundary condition, because it requires the mesh of the corresponding flow domain to be updated at every simulation step, as it also requires the initial conditions for each time step to be computed using interpolation (or extrapolation) from information of previous time steps. Therefore, a specific technique to deal with these issues must be implemented from the mesh-based methods available, e.g., overset grid, immersed boundary, boundary element, dynamic mesh, and level-set, et cetera. Here, we use the overset grid method. Notice that the technical literature describes the implementation of a significant number of simulations based on quasi-steady blade-element formulations and on Navier-Stokes solvers, with diverse degrees of fidelity, in order to study the lift mechanisms and the aerodynamic forces generated by flapping wings with fully prescribed kinematics[21,22,23,24]. However, to this date, the use of integrated (rigid dynamics + CFD) simulations aiming to understand the complex dynamical behavior of wings that simultaneously actively flap and passively pitch has not been sufficiently investigated. Thus, an important objective of this work is to generate the analytical and simulation tools required to implement numerical solutions in the very challenging case in which a wing actively flaps and passively pitches.

A blade-element-based method, common in quasi-steady analyses, is used in Ref. 15 to analyze the passive-pitching rotation of a wing, using empirical formulas for the estimation of local lift and drag forces. In that work, a reasonable agreement between experiments and numerical simulations is achieved, evidenced through test cases, where the experimental and simulated average lift forces and resulting measured and simulated wing-pitching angles are compared. Considering that in that case the simulation's characteristic coefficients and empirical formulas used in the interpretation of sensors' measurements were distilled from experimental data obtained at similar Reynolds numbers, the relatively *good* matching between the signals estimated with the blade-element method and the experimentally measured signals is expected and unsurprising. Therefore, a similar simulation approach is expected to fail if applied to a broader range of cases (regimes) with different Reynolds numbers and diverse wing planforms, as in Ref. 15 the characteristic parameters used in the simulations, such as maximum lift and the location of the center of aerodynamic forces, were determined experimentally. In general, it is obvious that errors in the experimental estimation of model coefficients will greatly diminish the accuracy and reliability of the simulations. Similarly, errors in the estimation of the calibration and tuning constants used in the measurement of physical variables will negatively impact the accuracy and reliability of the experimental data, mainly instantaneous lift and drag forces, used in the validation of the numerical simulations. Thus, even though the blade-element-based quasi-steady method has been demonstrated effective in integrated simulations of flapping-wing systems, numerical reliability issues prevent this approach from being extended to a broader gamut of design and simulation situations.

In a different approach to that of Ref. 15, in Ref. 16, a 2-D solver based on a discontinuous Galerkin method was implemented to compute the instantaneous lift and drag forces generated through fully prescribed flapping and pitching kinematics, previously obtained from passive wing-pitching experiments. The results published therein indicate a significantly better degree of agreement between simulations and experimental data, when compared to the results obtained with quasi-steady methods like the one in Ref. 15. However, it is important to mention that even though 2-D simulations can be effective in predicting forces in certain cases, some researchers have argued that wrong vortex shedding information observed in the translational case is expected to appear in the flapping-wing case as well[22], and therefore, force predictions numerically computed using 2-D CFD methods cannot be considered highly reliable *a priori* by hypothesis. Also, similarly to the blade-element-based quasi-steady method case, 2-D CFD simulations require the utilization of some characteristic parameters highly difficult to estimate, such as the aerodynamic wing-mean-chord[25]. Furthermore, the reported congruence between 2-D and *three-dimensional* (3-D) force predictions for Reynolds numbers on the range $\left[10^2, 10^4\right]$ might only be valid for the physical case without spanwise translational velocity difference[25]. Thus, for a flapping-wing motion with spanwise local translational velocity gradient, the uncertainty regarding the similarity between 2-D and 3-D results and the selection of the characteristic chord preclude the application of 2-D simulations to more sophisticated flapping wing cases, such as when unorthodox wing planform shapes are considered.

The issues relating to the applicability and reliability of blade-element-based methods and 2-D numerical aerodynamic solvers indicate that more general methods for analysis and simulation of the passive wing-pitching phenomenon should be explored and developed. Three-dimensional Navier-Stokes equations are the natural way to describe fluidic phenomena. Consequently, if hardware and software computational requirements are available, Navier-Stokes simulations can be implemented without the need for the use of empirically-estimated characteristic parameters relating to the wing's size and local forces, reasons for which we adopt a 3-D simulation approach. One major question that still remains when 3-D simulations are used in the case considered in this paper is whether the integrated simulation can achieve convergence in the presence of numerical oscillations and numerical noises. In Ref. 20, the sequential numerical solution of equations of motion and 3-D Navier-Stokes equations was demonstrated feasible in the context of nonlinear flight dynamical analysis of flapping wing air vehicles which use active wing-pitching mechanisms. Here, we extend the sequential simulation approach in Ref. 20 to the passive wing-pitching case, which is the main interest of the research discussed in this paper. Notice that if the wing dynamics are treated as a subsystem of an entire MAV, it is reasonable to expect that a sequentially integrated simulation of an actively-flapping and passively-pitching wing should also work.

The methodology proposed in this paper allows one to address the fluid-structure interaction problem that arises when the dynamics of an actively-flapping and passively-pitching wing are considered, under the assumptions of a low Reynolds number, a perfectively rigid wing, and a vehicle in perfect normal hovering flight. Specifically, we formulate an integrated simulation approach in which the flexure hinge of the passively rotating mechanism is modeled using single-axis bending beam theory, the dynamical equations of the assumed perfectly rigid and thin moving wing are found using the Euler-Lagrange method in Kane's formulation, and the aerodynamic forces and moments acting on the wing's surfaces are computed with the use of a 3-D Navier-Stokes solver (STAR-CCM+). The proposed simulation strategy consists of solving the wing's dynamical equations of motion and the Navier-Stokes equations alternatingly in time, using an incomplete modified ODE-Euler scheme and the SIMPLE[a] algorithm. The suitability of the proposed integrated approach is verified for both the active and passive wing-pitching cases, through comparison of the simulation results with the experimental data available in the literature, specifically those in Ref. 15. Additionally, relevant variables for the evaluation of the aerodynamic performance, including the center of pressure location and power consumption, and the effects of wing properties such as hinge stiffness and wing planform are discussed. The presented results illustrate the potential and applicability of the proposed integrated simulation approach to the analysis and design of flapping-wing micro air vehicles.

The rest of the paper is organized as follows. Section II describes the dynamical modeling of the actively-flapping–passively-pitching wing system studied during the course of the presented research, Section III presents the proposed dynamical simulation approach and discusses some cases used for validation of the numerical methods and Section IV discusses the broader implications and applicability of the proposed modeling and simulation methods. Lastly, some conclusions and future research directions are drawn in Section V.

[a]Semi-Implicit Method for Pressured-Linked Equations.

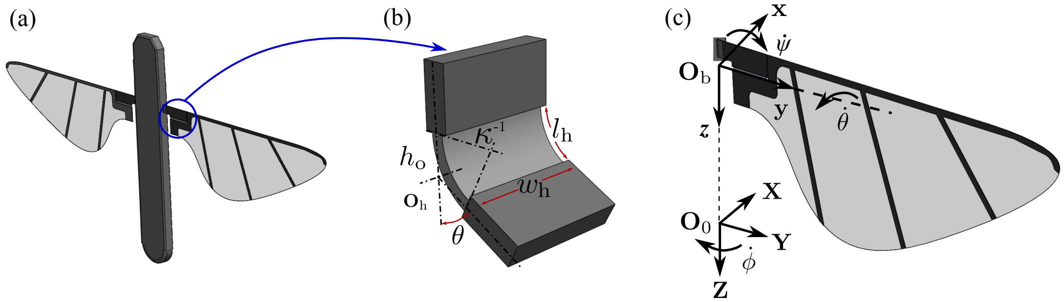

Figure 1. Dynamical flapping-wing system. (a) Illustration of the generic flapping-wing *micro air vehicle* (MAV) considered in this research. **(b)** Geometric model of the flexure hinge mechanism used for passive wing-pitching rotation. **(c)** Definition of the systems of coordinates. The inertial frame $\mathbb{F}_0$ is defined by the fixed axes $\{\mathbf{X}, \mathbf{Y}, \mathbf{Z}\}$ and the fixed origin $\mathbf{O}_0$, which coincides with the rotation point of the wing (shown displaced for illustrative purposes). Similarly, the wing-fixed (body) frame $\mathbb{F}_{\rm b}$ is defined by the axes $\{\mathbf{x}, \mathbf{y}, \mathbf{z}\}$ and the origin $\mathbf{O}_{\rm b}$.

II. DYNAMICAL MODELING

In this paper, we consider the dynamics of generic insect-scale flapping-wing MAVs of the kind depicted in Fig. 1, assuming the same basic aerodynamic and robotic designs to those of the prototypes in Refs. 1, 7, 9, 10, 11. Typically, systems of this kind are composed of an airframe, a pair of power actuators, a pair of mechanical transmissions and a pair of flexure hinges that connect the wings through the transmissions to the power actuators, which basically represent the basic conceptual design first developed at the Harvard Microrobotics Laboratory[1]. In the specific schemes employed in Refs. 1, 7, 9, 10, 11 and references therein, biomorph piezoelectric actuators generate linear motions that mechanical transmissions transform into the flapping motions ϕ, graphically described in Fig. 1. Thus, from the dynamical modeling and CFD perspectives, the angular trajectory ϕ is fully prescribed. In contrast, the wing-pitching motion θ is passively generated by inertial forces and the interaction of the flapping wing with the surrounding air, as the flexure hinge bends. The wings are assumed to be made of polyester film and reinforced with carbon fiber structures and considered to behave as thin rigid plates[15]. Also, the generic studied flapping-wing MAV is assumed to be in a perfect hovering state, or equivalently, attached to the ground.

In the dynamical modeling discussed here, two coordinate frames are defined to describe the motion of the wing. $\mathbb{F}_0\{\mathbf{O}_0, \mathbf{X}, \mathbf{Y}, \mathbf{Z}\}$ denotes an inertial frame of reference, which has its origin coinciding with the wing rotation point, its axis $\mathbf{Z}$ defined vertically downwards and axes $\mathbf{X}$ and $\mathbf{Y}$ perpendicular to $\mathbf{Z}$ and to each other, as shown in Fig. 1-(a) and Fig. 1-(c). Similarly, $\mathbb{F}_{\rm b}\{\mathbf{O}_{\rm b}, \mathbf{x}, \mathbf{y}, \mathbf{z}\}$ denotes a wing-fixed (body) frame with the same origin as that of $\mathbb{F}_0$, with its axis $\mathbf{y}$ extending along the flexure hinge center line, its axis $\mathbf{x}$ normal to the wind plane and its axis $\mathbf{z}$ downwards coinciding with $\mathbf{Z}$, as shown in Fig. 1-(c). Notice that in this case $\mathbb{F}_0$ and $\mathbb{F}_{\rm b}$ can be defined this way because in a perfect hovering state (or grounded), the robot remains fixed with respect to the ground. The relative attitude of the wing (and the wing-frame $\mathbb{F}_{\rm b}$) with respect to the vehicle's body (and the inertial frame $\mathbb{F}_0$) is described by the Euler angles $\{\phi, \theta, \psi\}$, representing the wing flapping, pitching and rolling angular motions about $\mathbf{Z}$, $\mathbf{y}$ and $\mathbf{x}$, respectively. Assuming a perfectly horizontal wing stroke plane, it immediately follows that ψ and $\dot{\psi}$ can be considered to be zero (or very small), which significantly simplifies the notation and analysis.

As graphically described in Fig. 1-(b), the flexure hinge employed to create the passive-pitching mechanism is treated as a simple single-axis bending beam with one face fixed to the driving spar, deforming according to a circular arc, as shown in Fig. 1-(b) and modeled in Refs. 15, 17, 18. Thus, from Hooke's law and the definition of strain, the curvature of the flexure neutral surface can be computed as $\kappa = M_{\rm h}(EI_{\rm h})^{-1}$, where $M_{\rm h}$ is the externally applied moment to the beam, E is the elastic modulus of the hinge material and $I_{\rm h}$ is the second moment of area of the hinge transverse section. For the deformation in Fig. 1-(b) (circular arc), the deflection angle of the flexure hinge is $\theta = \kappa l_{\rm h}$, where $l_{\rm h}$ is the length of the flexural element, which implies that the magnitude of the external moment applied to the bending beam can be computed as $M_{\rm h} = EI_{\rm h}\theta l_{\rm h}^{-1}$. For the rectangular section in Fig. 1-(b), with width $w_{\rm h}$ and thickness $\tau_{\rm h}$, the second moment of area is $I_{\rm h} = 12^{-1} \cdot w_{\rm h}\tau_{\rm h}^3$. It follows that the equivalent torsional stiffness of the flexure hinge element can be computed as

$$k_{\rm h} = \frac{EI_{\rm h}}{l_{\rm h}} = \frac{Ew_{\rm h}\tau_{\rm h}^3}{12 l_{\rm h}}. \tag{1}$$

The last piece required to complete the modeling of the flexure hinge is the position of the equivalent rotation axis of the wing, which is necessary to determine the exact instantaneous attitude of the wing in space. In this case, directly from Fig. 1-(b), it follows that the critical parameter that determines the position of the wing's rotation axis, the distance h_{o} in Fig. 1-(b), is given by

$$h_{\mathrm{o}} \approx \frac{1}{\kappa} \sin \frac{\theta}{2} = \frac{l_{\mathrm{h}}}{\theta} \sin \frac{\theta}{2}. \tag{2}$$

Thus, taking into account the maximum possible geometric deflection of the hinge and the relatively small value of l_{h} compared to the wing chord, the rotation axis shift during wing-pitching is relatively small, and therefore, negligible. Consistently, in this paper, the flexure hinge is modeled as a linear torsional spring rotating about an equivalent rotation axis located at a distance $0.5 \cdot l_{\mathrm{h}} \approx h_{\mathrm{o}}$ from the top end of the rectangular flexure element, as drawn in Fig. 1-(b), with a constant stiffness k_{h}.

Having found a mathematical description for the flexure hinge, now we find the dynamical equations of motion for the actively-flapping–passively-pitching wing under consideration. For the flapping-wing MAV shown in Fig. 1, in perfect hovering (or fixed to the ground), the wing motion can be completely described by the set of Euler angles $\{\phi, \theta, \psi\}$ that relate the frames $\mathbb{F}_0$ and $\mathbb{F}_{\mathrm{b}}$ to each other, as shown in Fig. 1-(c). As explained above, for a perfectly horizontal stroke plane, the rolling motion of the wing is constant and zero, i.e., $\psi = \dot{\psi} = 0$, which implies that the angular velocity of the wing can be expressed as

$$\boldsymbol{\omega} = \dot{\phi}\mathbf{e_Z} + \dot{\theta}\mathbf{e_y} = -\dot{\phi}\sin\theta\mathbf{e_x} + \dot{\theta}\mathbf{e_y} + \dot{\phi}\cos\theta\mathbf{e_z}, \tag{3}$$

when employed in the determination of the wing dynamics.

From the rigid wing assumption[15], for the actively-flapped–passively-pitching wing considered here, it follows that the equations of motion can be derived employing the Euler-Lagrange method in Kane's formulation for generalized forces[26],

$$\frac{\mathrm{d}}{\mathrm{d}t}\left(\frac{\partial L}{\partial \dot{q}}\right) - \frac{\partial L}{\partial q} = \sum_{i=1}^{N_{\mathrm{c}}} \mathbf{F}_i \cdot \frac{\partial \mathbf{v}_i}{\partial \dot{q}} + \sum_{i=1}^{N_{\mathrm{c}}} \mathbf{M}_i \cdot \frac{\partial \boldsymbol{\omega}_i}{\partial \dot{q}}, \tag{4}$$

where, on the left-hand side, L is the Lagrangian, q is a generic generalized coordinate and $\dot{q}$ is a generic generalized velocity, i.e., the derivative of q with respect to time, denoted by t. On the right-hand side, N_c denotes the total number of rigid elements composing the mechanical system, $\mathbf{v}_i$ is the velocity of the center of mass of the ith rigid element and $\boldsymbol{\omega}_i$ is the angular velocity of the ith rigid element. The other variables required for the computation of the generalized forces on the right-hand side of Eq. (4) are the active forces and moments acting on the linkage system. Here, $\mathbf{F}_i$ is the total active force applied at the center of mass of the ith rigid element of the mechanical system and $\mathbf{M}_i$ is the total active moment applied about the center of mass of the ith rigid element of the mechanical system. If an active force applied to the ith component does not pass through the corresponding center of mass, an equivalent force $\mathbf{F}_i$ and an equivalent moment $\mathbf{M}_i$ acting on the center of mass of the ith rigid element need to be obtained by shifting the point of action. In the case considered here, shown in Fig. 1, we select ϕ and θ as the generalized coordinates, and $\dot{\phi}$ and $\dot{\theta}$ as the generalized velocities of the passively-rotating flapping-wing system. For wings fabricated with polyester film and reinforced with carbon fiber structures, as those in Refs. 7, 15, it is reasonable to treat the wing as a thin plate, and therefore, the moment of inertia matrix with respect to the frame $\mathbb{F}_{\mathrm{b}}$,

$$\mathrm{J_b} = \begin{bmatrix} J_x & J_{xy} & J_{xz} \\ J_{xy} & J_y & J_{yz} \\ J_{xz} & J_{yz} & J_z \end{bmatrix}, \tag{5}$$

is assumed to satisfy $J_{xy} \approx J_{xz} \approx 0$ and $J_x \approx J_y + J_z$[15]. Additionally, since the stroke plane is assumed to be perfectly horizontal and the wing is assumed to be made of lightweight material, the change in gravitational potential energy of the system is neglected in this analysis, and consequently, in the construction of the Lagrangian L, we consider the hinge potential energy only. Thus, in order to find L, we write the kinetic energy K and the potential energy V, as

$$K = \frac{1}{2}\boldsymbol{\omega}^T \mathrm{J_b} \boldsymbol{\omega} = \frac{1}{2}(\dot{\phi}^2 \sin^2\theta + \dot{\theta}^2) J_y + \dot{\phi}\dot{\theta}\cos\theta J_{yz} + \frac{1}{2}\dot{\phi}^2 J_z, \tag{6}$$

$$V = \frac{1}{2} k_{\mathrm{h}} \theta^2. \tag{7}$$

Once again, notice that in the expression for V, we have neglected the gravitational component of the potential energy, for reasons already explained above.

Recalling that the Lagrangian is $L = K - V$, it follows that for the generalized coordinate θ, the aggregated generalized inertial and conservative active forces in Eq. (4), i.e., the *left-hand side* (LHS) of Eq. (4) for θ, are given by

$$\mathrm{LHS}_\theta = \frac{\mathrm{d}}{\mathrm{d}t}\left(\frac{\partial L}{\partial \dot{\theta}}\right) - \frac{\partial L}{\partial \theta} = J_y \ddot{\theta} + J_{yz}\ddot{\phi}\cos\theta - \frac{1}{2}J_y\dot{\phi}^2\sin 2\theta + k_\mathrm{h}\theta. \tag{8}$$

In this case (wing in Fig. 1-(c)), the non-conservative active forces include, as the major contributors, the total aerodynamic force distribution acting on the wing's surfaces (aerodynamic force for short) and the torque driving the wing flapping about the axis $\mathbf{Z}$. As explained later in Section III.A, aerodynamic forces acting on the wing are generated mainly by pressure differences between the two main flat surfaces of the wing, and therefore, the viscous shear-stresses on the wing's surfaces can be neglected. Also, it can be shown that the aerodynamic force distribution acting on the wing's surfaces can be aggregated using numerical integration in order to obtain an equivalent total aerodynamic force, $\mathbf{F}_\mathrm{c}$, applied at the wing's center of mass and an equivalent total aerodynamic moment, $\mathbf{M}_\mathrm{c}$, applied about the wing's center of mass. Furthermore, from $\mathbf{F}_\mathrm{c}$ and $\mathbf{M}_\mathrm{c}$, an equivalent total aerodynamic moment about the fixed point $\mathbf{O}_\mathrm{b}$, $\mathbf{M}_\mathrm{ae}$, can be found with the use of basic vector calculus, noticing that

$$\begin{aligned}
\mathbf{F}_\mathrm{c} \cdot \frac{\partial \mathbf{v}_\mathrm{c}}{\partial \dot{\theta}} + \mathbf{M}_\mathrm{c} \cdot \frac{\partial \boldsymbol{\omega}}{\partial \dot{\theta}} &= \mathbf{F}_\mathrm{c} \cdot \frac{\partial (\boldsymbol{\omega} \times \mathbf{r}_\mathrm{c})}{\partial \dot{\theta}} + \mathbf{M}_\mathrm{c} \cdot \frac{\partial \boldsymbol{\omega}}{\partial \dot{\theta}} \\
&= \mathbf{F}_\mathrm{c} \cdot \left(\frac{\partial \boldsymbol{\omega}}{\partial \dot{\theta}} \times \mathbf{r}_\mathrm{c}\right) + \mathbf{M}_\mathrm{c} \cdot \frac{\partial \boldsymbol{\omega}}{\partial \dot{\theta}} \\
&= \left(\mathbf{r}_\mathrm{c} \times \mathbf{F}_\mathrm{c} + \mathbf{M}_\mathrm{c}\right) \cdot \frac{\partial \boldsymbol{\omega}}{\partial \dot{\theta}} \\
&= \mathbf{M}_\mathrm{ae} \cdot \frac{\partial \boldsymbol{\omega}}{\partial \dot{\theta}}.
\end{aligned} \tag{9}$$

That is, from Eq. (9) the equivalent total aerodynamic moment about the fixed point $\mathbf{O}_\mathrm{b}$ can be computed as $\mathbf{M}_\mathrm{ae} = \mathbf{M}_\mathrm{c} + \mathbf{r}_\mathrm{c} \times \mathbf{F}_\mathrm{c}$, where $\mathbf{r}_\mathrm{c}$ is the position vector of the wing's center of mass measured from the fixed point $\mathbf{O}_\mathrm{b}$. Notice that in this case, $\mathbf{r}_\mathrm{c}$ does not depend directly on $\dot{\theta}$, and accordingly, the *right-hand side* (RHS) of Eq. (4) for θ, i.e., the generalized non-conservative moment associated with the generalized coordinate θ, becomes

$$\mathrm{RHS}_\theta = \left(\begin{bmatrix} M_{\mathrm{ae},\mathbf{x}} \\ M_{\mathrm{ae},\mathbf{y}} \\ M_{\mathrm{ae},\mathbf{z}} \end{bmatrix} + \begin{bmatrix} -M_\mathrm{drv}\sin\theta \\ 0 \\ M_\mathrm{drv}\cos\theta \end{bmatrix}\right) \cdot \frac{\partial \boldsymbol{\omega}}{\partial \dot{\theta}} = M_{\mathrm{ae},\mathbf{y}}, \tag{10}$$

where $\{M_{\mathrm{ae},\mathbf{x}}, M_{\mathrm{ae},\mathbf{y}}, M_{\mathrm{ae},\mathbf{z}}\}$ are the components of the total aerodynamic moment vector $\mathbf{M}_\mathrm{ae}$, written with respect to the body frame $\mathbb{F}_\mathrm{b}$ and M_drv is the magnitude of the driving torque about the axis $\mathbf{Z}$. For consistency, in order for Eq. (10) to work, all the vectors must be expressed with respect to the same frame of reference, in this case $\mathbb{F}_\mathrm{b}$. Since the term M_drv does not appear in the final expression of the generalized force associated with the generalized coordinate θ, it follows that the driving torque does not directly affect the generalized coordinate θ, and therefore, ϕ and $\dot{\phi}$ can be considered as completely prescribed inputs to Eq. (8). Then, substituting Eq. (8) and Eq. (10) into Eq. (4), the second-order equation describing the motion of the wing-pitching angle θ can be written as

$$J_y\ddot{\theta} = \tilde{M}_\theta - J_{yz}\ddot{\phi}\cos\theta + \frac{1}{2}J_y\dot{\phi}^2\sin 2\theta, \tag{11}$$

where $\tilde{M}_\theta = M_{\mathrm{ae},\mathbf{y}} - k_\mathrm{h}\theta$ is the pitching moment about the axis $\mathbf{y}$, including the aerodynamic moment and the hinge restoring moment. Employing the same general methodology, we derive the governing equation associated with the generalized coordinate ϕ, which in this case becomes

$$\ddot{\phi}\left(J_y\sin^2\theta + J_z\right) = \tilde{M}_\phi - \dot{\phi}\left(J_y\dot{\theta}\sin 2\theta\right) - J_{yz}\left(\ddot{\theta}\cos\theta - \dot{\theta}^2\sin\theta\right), \tag{12}$$

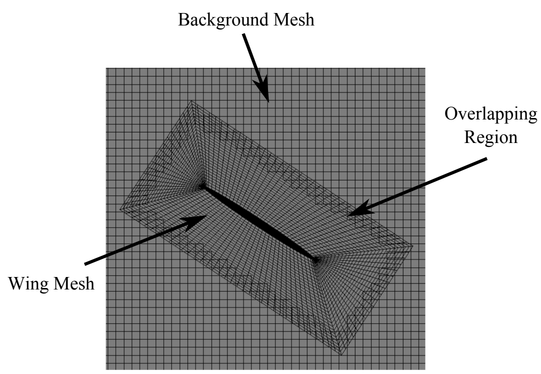

Figure 2. Example of overset grid assembly for a 3-D rotating wing, which defines a moving boundary, with structured mesh domains. Three kinds of distinctive time-varying mesh domains are defined. A first mesh domain is defined for the background flow field (background mesh). A separate mesh domain is defined for the solid object immersed in the fluid (wing mesh). A transitional overlapping region is defined to coherently connect the background and object mesh domains to each other.

with $\tilde{M}_\phi = M_{\mathrm{ae},\mathbf{Z}} + M_{\mathrm{drv}}$, where $M_{\mathrm{ae},\mathbf{Z}}$ is the component of $\mathbf{M}_{\mathrm{ae}}$ along axis $\mathbf{Z}$ of $\mathbb{F}_0$ and M_{drv} is the same term in Eq. (10). As extensively discussed in Refs. 4, 5, 7, 27, for the kinds of driving mechanisms considered here, controllers can be designed to accurately follow desired flapping trajectories, and consequently, in this work, ϕ is considered to be fully prescribed. Consequently, as ϕ is assumed to be completely determined *a priori*, in all the analyses and simulations presented in this paper, Eq. (12) is used to evaluate the applied torque on the driving spar of the wing. Notice that the Euler-Lagrange-Kane method employed in this section is an alternative to the approach reported in Ref. 15, which uses the Newton-Euler laws of motion and blade-element analysis to find the dynamics of passively-pitching flapping wings.

III. SIMULATIONS AND VALIDATION

In this section, we present the proposed integrated numerical method for the simulation of the actively-flapping–passively-pitching wing, graphically described in Fig. 1, and discuss some cases used in the validation of the numerical methods and simulation approach as a whole.

III.A. Simulation Methods

In the previous section, the equations of motion for the actively-flapping–passively-pitching wing were derived using the Euler-Lagrange method in Kane's formulation. As explained above, the dynamics described by Eq. (11) cannot be solved analytically because in this formulation the input $M_{\mathrm{ae},\mathbf{y}}$ is unknown *a priori*. Therefore, to find a numerical solution to Eq. (11), an updated total aerodynamic moment $\mathbf{M}_{\mathrm{ae}}$ needs to be computed at each simulation step. Since $\mathbf{M}_{\mathrm{ae}}$ represents the aggregated effects of the distributed aerodynamic pressure and the distributed shear-stress on the wing, the flow field surrounding the wing's surfaces is required at each simulation step and computed numerically. In this case, the continuum air flow around the wing of the considered generic insect-scale flapping-wing MAV (graphically described in Fig. 1) is three-dimensional and unsteady with low Reynolds numbers associated to it, here described employing the 3-D incompressible Navier-Stokes equations[20],

$$\nabla \cdot \mathbf{u} = 0, \tag{13}$$

$$\frac{\partial \mathbf{u}}{\partial t} + \mathbf{u} \cdot \nabla \mathbf{u} = -\frac{1}{\rho}\nabla p + \nu \nabla^2 \mathbf{u}, \tag{14}$$

which in this work are solved numerically, employing an implicit unsteady segregated flow solver, based on the finite volume method with the STAR-CCM+ package. As usual, in Eqs. (13) and (14), $\mathbf{u}$ is the velocity of the air flow field, p is the pressure of the air flow field and ρ is the density of the air. A major challenge that arises in the 3-D simulation of flapping wings is that the airflow surrounding the wing's surfaces is constrained by time-varying moving boundaries, and therefore, from a numerical perspective, the computation of the instantaneous total aerodynamic moment, $\mathbf{M}_{\mathrm{ae}}$, at each simulation step requires the numerical solution of a set of partial differential equations with a new boundary condition for each time step (moving boundary condition for short). In the cases studied in this paper, the moving boundary determined by the rotating

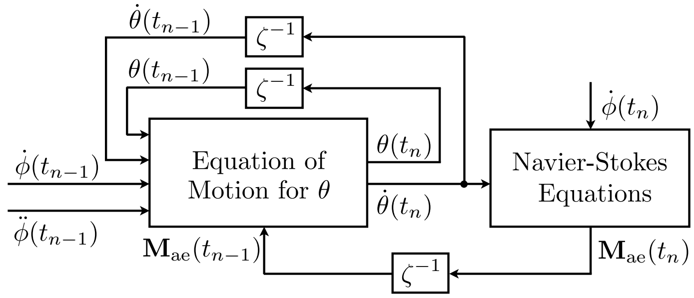

Figure 3. Data-flow diagram of the proposed integrated simulation method. In this scheme, the dynamic equation associated with the generalized coordinate θ and the Navier-Stokes equations are solved alternatingly to numerically estimate the complete dynamical behavior of an actively-flapping and passively-pitching wing. Here, ζ^{-1} denotes the unit delay operator, such that for the discrete-time signal $\theta(t_n)$, its follows that $\theta(t_{n-1}) = \zeta^{-1}\theta(t_n)$.

wing in space is dealt with numerically by employing the overset grid technique available in STAR-CCM+, as exemplified with the airfoil shown in Fig. 2. When the overset grid method is employed, three kinds of distinctive time-varying meshes are defined. A first mesh domain is defined for the background flow field and separate mesh domains, typically thiner, are defined for the solid objects submerged in the fluid, as done for the airfoil in Fig. 2. Also as exemplified in Fig. 2, a transitional overlapping region is required to coherently connect the background and object mesh domains to each other. In general, each object domain can be assigned either with *a priori* fully prescribed, or alternatively instantaneous, motion trajectories. In this work, all the mesh domains, including the background mesh, are assembled together dynamically during the simulation process and the physical quantities in the different mesh domains are exchanged and interpolated in the overlapping regions.

Once the Navier-Stokes equations are solved in the discretized space, the spatial distributions of pressure and velocity can be computed, and consequently, the magnitudes of aerodynamic forces in any direction $\mathbf{l}_F$ and moments about any axis $\mathbf{l}_M$ can be evaluated by aggregating the pressure distribution and shear-stress distribution over the boundary surface of the flapping wing, using discrete integration as

$$F_{\rm ae,\mathbf{l}} = \sum_{i=1}^{N_{\rm e}} (\mathbf{f}_{{\rm pres},i} + \mathbf{f}_{{\rm shear},i}) \cdot \mathbf{l}_F, \tag{15}$$

$$M_{\rm ae,\mathbf{l}} = \sum_{i=1}^{N_{\rm e}} \{\mathbf{r}_i \times (\mathbf{f}_{{\rm pres},i} + \mathbf{f}_{{\rm shear},i})\} \cdot \mathbf{l}_M, \tag{16}$$

where $\mathbf{f}_{{\rm pres},i} = (p_i - p_{\rm ref}) \cdot \mathbf{a}_i$ is the normal pressure force on the ith surface element (computed using the absolute pressure on the ith surface element, p_i, and the reference pressure, $p_{\rm ref}$), $\mathbf{f}_{{\rm shear},i} = -\mathbf{T}_i \cdot \mathbf{a}_i$ is the shear-stress force on the ith surface element, $\mathbf{r}_i$ marks the position of the ith element from the fixed point $\mathbf{O}_{\rm b}$, $\mathbf{a}_i$ is the normal vector area associated with the ith surface element, $\mathbf{T}_i$ is the shear-stress tensor on the ith surface element and $N_{\rm e}$ is the total number of elements composing the boundary surface[28]. Since the shear-stress force is small compared to the pressure force and the wing is modeled as a thin plate, the contribution of the shear-stress to the aerodynamic moment is considered negligible. Thus, only the pressure force and moment coming from the pressure difference between the two main flat surfaces of the wing are modeled as active aerodynamic variables acting on the wing's structure, when the formulation given by Eqs. (9), (10), (11) and (12) is considered.

Once the aerodynamic moment $\mathbf{M}_{\rm ae}$ has been obtained, the dynamics associated with the generalized coordinate $\theta(t)$ are solved numerically by employing a discretized model of Eq. (11) in a time marching process that yields the discrete-time series $\theta(t_n)$ and $\dot{\theta}(t_n)$, as schematized in the data-flow diagram of Fig. 3. In this scheme, t_n is the time in seconds associated with the simulation step n, ζ^{-1} is the discrete-time delay operator, and $\theta(t_{n-1})$, $\dot{\theta}(t_{n-1})$, $\dot{\phi}(t_{n-1})$, $\ddot{\phi}(t_{n-1})$ and $\mathbf{M}_{\rm ae}(t_{n-1})$ are the inputs to the block that computes $\theta(t_n)$ and $\dot{\theta}(t_n)$. Similarly, $\dot{\theta}(t_n)$ and $\dot{\phi}(t_n)$ are the inputs to the block that computes $\mathbf{M}_{\rm ae}(t_n)$ by numerically solving the Navier-Stokes in Eq. (13), as explained above. Clearly, the flow of information in Fig. 3 defines an alternating procedure in which the Navier-Stokes equations are used to estimate the aerodynamic moment $\mathbf{M}_{\rm ae}$, and then, using this information, the rigid dynamical equation of the wing-pitching motion is solved in order to update the moving boundary condition defined by the moving wing, as proposed for the general flapping case in Ref. 20. In the scheme of Fig. 3, the process of numerically determining a solution for the second-order ODE in Eq. (11) is implemented with the set of first-order equations

$$\dot{\theta} = \mu, \tag{17}$$

$$\dot{\mu} = G(t, \theta, \dot{\phi}, \ddot{\phi}, M_{\mathrm{ae},\mathbf{y}}, J_y) = \Pi_{\mathrm{ae}} + g(t, \theta, \dot{\phi}, \ddot{\phi}), \tag{18}$$

where $\Pi_{\mathrm{ae}} = M_{\mathrm{ae},\mathbf{y}} J_y^{-1}$ and $g(t, \theta, \dot{\phi}, \ddot{\phi}) = -k_{\mathrm{h}} \theta J_y^{-1} - J_{yz} \ddot{\phi} J_y^{-1} \cos\theta + 2^{-1} \cdot \dot{\phi}^2 \sin 2\theta$. By inspection, it seems that Eqs. (17) and (18) can be easily solved using standard numerical integration techniques for the solution of ODEs, such as the ODE-Euler or Runge-Kutta methods. However, a major difficulty that appears here is that first-order accuracy requires very small simulation steps to achieve acceptable numerical precision, and if higher-order schemes are employed, the expression $\dot{\mu} = \Pi_{\mathrm{ae}} + g(t, \theta, \dot{\phi}, \ddot{\phi})$ cannot be evaluated properly for simulation sub-steps, because the aerodynamic moment $M_{\mathrm{ae},\mathbf{y}}$ does not have an explicit expression. This difficulty can be addressed by implementing multiple-step recursive simulation processes, where the aerodynamic expression Π_{ae} is predicted *a priori* for step $n+1$, using information available at step n, and corrected *a posteriori* for step $n+1$, using information available at step $n+1$. Unfortunately, such an approach requires significant computational resources, making the whole simulation more expensive and slower. An alternative approach, the one followed here, is the implementation of an incomplete modified ODE-Euler method in which the aerodynamic quantity Π_{ae} computed at step n (time t_n) is assumed to remain constant from t_n to t_{n+1} and not corrected *a posteriori*. Then, the expression

$$G^* = \Pi_{\mathrm{ae}}(t_n) + g(t_{n+1}, \theta^*, \dot{\phi}(t_{n+1}), \ddot{\phi}(t_{n+1})) \tag{19}$$

is employed to compute an approximated numerical solution of Eq. (11), where θ^* and G^* can be thought of as *a priori* predictions of $\theta(t_{n+1})$ and $G(t_{n+1})$, respectively. Since the flapping angle ϕ is prescribed, unlike Π_{ae}, which is kept constant from t_n to t_{n+1}, $\dot{\phi}$ and $\ddot{\phi}$ are updated at time t_{n+1}, before being used in the computation of the prediction of $G(t_{n+1})$. Thus, employing this proposed incomplete modified ODE-Euler scheme combined with the solver capabilities of the STAR-CCM+ package, the pair of Eqs. (13), (14) and the pair of Eqs. (17), (18) are alternatingly solved with the time marching strategy shown in Fig. 3, which is a simulation method that simultaneously integrates the rigid and fluid dynamics associated with the flapping-wing phenomenon. Some relevant simulation results are presented below.

III.B. Implementation and Simulation Results

In this section, the integrated simulation approach proposed in Section III.A, which combines the solution to the wing dynamics in Eq. (11) and the solution to the 3-D Navier-Stokes equations in Eqs. (13) and (14), is used to numerically simulate the behavior of a passively-pitching wing for a prescribed flapping motion ϕ. Compelling evidence demonstrating the suitability of the proposed approach is obtained by comparing the simulation results with the benchmark experimental cases published in Ref. 15. Here, the modified ODE-Euler scheme proposed in Section III.A is implemented using the user code tool of STAR-CCM+, which allows the exchange of data between the algorithms solving for the solid dynamics of the wing system and the STAR-CCM+ aerodynamic solver. In the research program presented in this paper, a step previous to the simulation of the passive-pitching case is the simulation of an active-pitching case (presented in Section III.B.1), in which the flapping-wing system is simulated employing fully prescribed flapping and pitching rotations in order to identify the role of inertial forces and also to assess the reliability and accuracy of the aerodynamic simulation schemes. In Section III.B.2, simulation results of the fully integrated passive-pitching case in Fig. 3 are presented, obtained by using a wing with the same geometry and prescribed flapping-wing motions used in the active-pitching case.

As mentioned above, the prescribed angular motions used in the simulations, for both the active-pitching case and the passive-pitching case, are generated using the experimental data published in Ref. 15. The experimental results in Ref. 15 were obtained through an experimental setup that combines passive optical components, high-speed cameras, custom-made force sensors, and computational processing to extract the instantaneous kinematics and lift forces, as graphically described in Fig. 4-(a), of the artificial wing in Fig. 4-(b), while actively flapping and passively pitching, as described in Section II. The artificial wing and the flapping pattern ϕ in Ref. 15, shown in Figs. 4-(b) and 4-(c), are biologically inspired by the wings and flying mechanisms of the species *Eristalis tenax* (drone fly) with the important difference that in the artificial case, the wing was strongly structurally reinforced with carbon fiber in order to make it as rigid as possible. In Ref. 15, the wing is driven by a piezoelectric bimorph actuator [1] and the resulting instantaneous forces

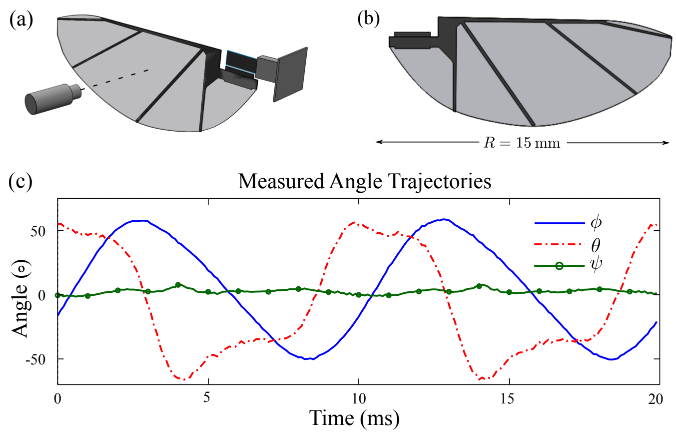

Figure 4. Benchmark experimental case. **(a)** Basic illustration of the experimental setup used in the obtention of the results in Ref. 15, used in this research for comparison and validation purposes. **(b)** Wing planform shape employed in the simulations and analyses presented here. **(c)** Actively prescribed experimental flapping motion ϕ, experimentally measured passive-pitching rotation θ and experimentally measured rolling motion ψ (courtesy of Dr. J. P. Whitney [15]).

are measured with a custom-made apparatus composed of a capacitive displacement sensor and an Invar double-cantilever beam, in an structural scheme in which using basic principles of solid mechanics, the beam deformation is mapped into a measurement of force. The attitude of the flapping wing is captured with a high-speed camera and an auxiliary mirror for stereoscopic reconstruction. As discussed in Ref. 5, sinusoidal inputs to the piezoelectrically actuated mechanisms in Refs. 1, 5, 15, and references therein, generate periodic (almost sinusoidal) flapping trajectories, and therefore, the mappings from actuator excitations to flapping angles ϕ can be considered to be *linear time-invariant* (LTI). In the particular case discussed in Ref. 15, the resulting flapping trajectories are quasi-sinusoidal periodic signals with a fundamental frequency equal to the actuator excitation frequency (100 Hz). An example showing the extracted wing kinematics is shown in Fig. 4-(c), where the signals of the rotation angles $\{\phi, \theta, \psi\}$ were estimated from captured images, using 2-D signal processing techniques, under the assumption of a perfectly flat and rigid wing. In this experimental example, the equivalent torsional stiffness coefficient of the flexure hinge is estimated to be $k_{\mathrm{h}} \approx 2.3520\ \mu\mathrm{Nm}\cdot\mathrm{rad}^{-1}$. At this point, it is important to mention that in this paper Euler angles are defined following the Z-Y-X convention, as in Ref. 15 Euler angles are defined according to the Z-X-Y convention. Also, notice that as in Ref. 15, the Euler angle about the instantaneous axis $\mathbf{x}$ in Fig. 1 is referred to as the deviation angle, while here we refer to it as the rolling angle ψ. Notice that the rolling angle ψ is important only in the evaluation of the vertical experimental inertial forces, and consequently, it is not of significant importance in the aerodynamic simulations discussed here, as perfectly horizontal stroke planes are assumed. Also, notice that from an experimental perspective, the rolling angle ψ is important in the estimation of inertial forces, but can be neglected in the experimental measurement of the flapping angle ϕ and the pitching angle θ, as ψ does not affect their experimental quantification.

Another experimental variable, besides the passive-pitching kinematics, used to compare and validate the proposed simulation method is the magnitude of the instantaneous measured total vertical force F_Z, which is the resultant vertical force component acting on the driving spar, including contributions due to aerodynamic forces, gravity and other inertial forces, i.e.,

$$F_Z = F_{\mathrm{L}} + m a_Z - m g, \tag{20}$$

where F_{L} is the total instantaneous vertical aerodynamic component (lift) in the opposite direction of $\mathbf{Z}$, a_Z is the vertical component of the wing's center of mass acceleration with respect to the inertial frame $\mathbb{F}_0$ and mg is the flyer's weight. The complete list of the wing parameters required for the implementation of the simulations presented here can be found in the appendix of Ref. 15. The active and passive simulations implemented in the course of the research discussed in this paper are discussed below.

III.B.1. Active-Pitching Simulation

To identify and characterize the importance of inertial forces in the dynamical behavior of the flapping wing and to validate the 3-D aerodynamic solver (STAR-CCM+), the first set of simulations performed during the course of this research were implemented with fully prescribed flapping and pitching motions,

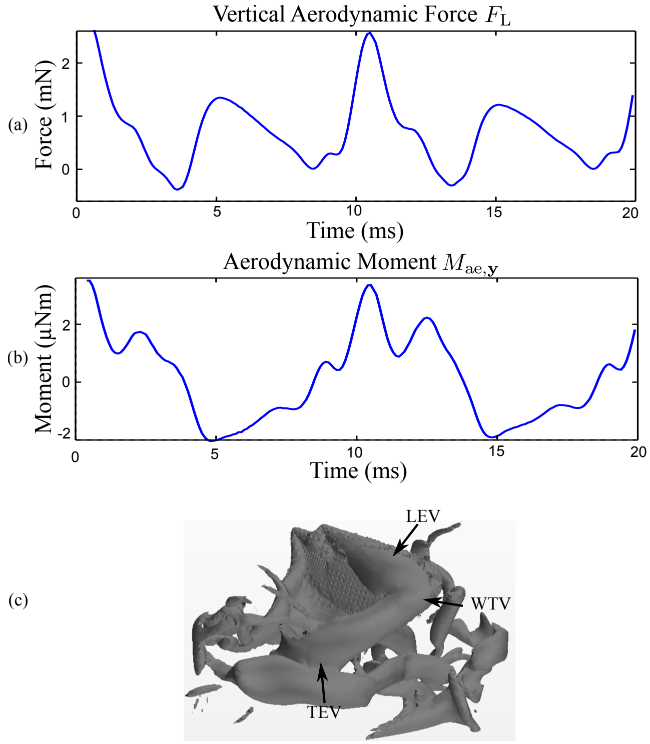

Figure 5. Aerodynamic simulation results of a flapping wing with fully prescribed wing-pitching rotation θ. Here, the prescribed motions θ and ϕ are taken from Ref. 15. **(a)** Magnitude of the simulated total instantaneous aerodynamic vertical force, F_{L} (lift). **(b)** Magnitude of the simulated total aerodynamic moment about axis $\mathbf{y}$, $M_{\mathrm{ae},\mathbf{y}}$. **(c)** Resulting spatial *leading-edge vortex* (LEV), *wing-tip vortex* (WTV) and *trailing-edge vortex* (TEV).

employing the ϕ and θ experimental signals shown in Fig. 4-(c), computed from the data in Ref. 15. We denote this kind of numerical implementation as an *active-pitching* simulation. As can be observed in Fig. 4-(c), since the rolling angle ψ is significantly smaller than the flapping and pitching angles, ϕ and θ, we consider it to be negligible, i.e., $\psi = 0$, for simulation purposes. Notice, however, that as explained later in this paper, the experimental signal ψ in Fig. 4-(c), despite of being small, cannot be neglected in the estimation of inertial forces from experimental data. Also, notice that in the active-pitching simulation case, discussed in this section, since the pitching angle θ is fully prescribed according to the signal in Fig. 4-(c), the dynamical equation Eq. (11) is not employed in the numerical implementation, the simulation process becomes purely aerodynamical, and therefore, the fluid-structure interaction phenomenon is not included. As mentioned before, active-pitching aerodynamic simulations (with fully prescribed kinematics) are relevant because they allows us to perform a first validation by comparing the magnitude of the simulated total vertical force to the magnitude of the experimentally measured total vertical force, published in Ref. 15. As already discussed in this paper, the total aerodynamic force acting on the wing can be computed by integrating the force distribution on the wing's surfaces, which is obtained from the numerical solution to the Navier-Stokes equations in Eqs. (13) and (14). Specifically, here we use the implicit unsteady segregated flow solver in STAR-CCM+ for a laminar flow model of the baseline case with a Reynolds number on the range $\left[10^2, 10^4\right]$. Additionally, in this simulation, in order to avoid numerical errors due to noise, signals ϕ and θ in Fig. 4-(c) are smoothed by filtering out high-frequency small-amplitude fluctuations by computing the Fourier series of the signals and then eliminating their high-order harmonics.

The simulation results for the active-pitching case studied in this section are summarized in Fig. 5. Here, Fig. 5-(a) shows the simulated magnitude of the total instantaneous vertical aerodynamic forces, F_{L}. Similarly, the simulated magnitude of the instantaneous y-component of the total aerodynamic moment $M_{\mathrm{ae},\mathbf{y}}$ and one resulting 3-D iso-vorticity surface are shown in Fig. 4-(b) and Fig. 4-(c), respectively. Notice that because the prescribed wing-flapping and and wing-pitching trajectories in Fig. 4 are not symmetrical with respect to zero, the resulting upstroke and downstroke total aerodynamic forces are not symmetric to each other with respect to the motion-reversal point either. Furthermore, the resulting upstroke and downstroke y-components of the aerodynamic moment are not symmetric to each other with respect to the motion-reversal point. Also, it is important to mention that the 3-D iso-vorticity surface has a similar

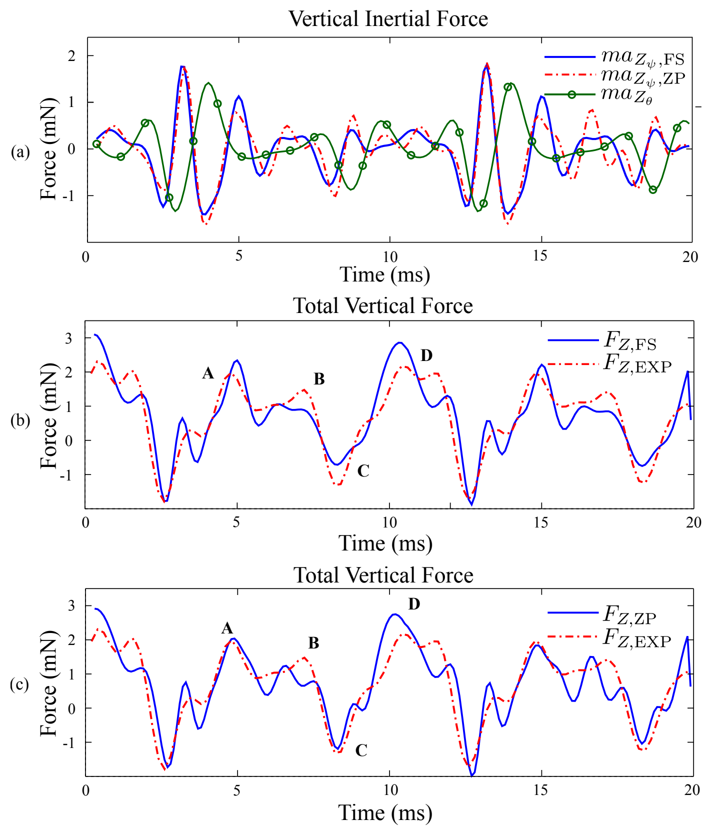

Figure 6. Hybrid estimation of the total instantaneous vertical force for the active wing-pitching case. (a) Components of the inertial force ma_Z, estimated from the experimentally measured flapping, pitching and rolling motions. **(b)** Hybridity estimated total vertical force $F_{Z,\mathrm{FS}}$, using Fourier series fitting, compared to the experimentally measured total vertical force $F_{Z,\mathrm{EXP}}$. **(c)** Hybridity estimated total vertical force $F_{Z,\mathrm{ZP}}$, using low-pass filtering, compared to the experimentally measured total vertical force $F_{Z,\mathrm{EXP}}$.

spatial structure, i.e., *leading-edge vortex* (LEV), *wing-tip vortex* (WTV) and *trailing-edge vortex* (TEV), to the spatial structure in Ref. 29, obtained experimentally using *digital particle image velocimetry* (DPIV) visualization techniques, which is a first indication on the correctness of the numerical solution. Further validation of the method is done by comparing the simulated signals to the experimentally measured ones.

As described in Eq. (20), the experimentally measured total vertical force, F_Z, is the sum of the total vertical aerodynamic force, F_L, the vertical inertial force, ma_Z, and the weight mg. Thus, in order to obtain F_Z from the simulation, mg is trivially calculated, F_L is computed as explained before from the solution to Navier-Stokes equations in Eqs. (13) and (14) and ma_Z is evaluated from the computation of a_Z with respect to the inertial frame $\mathbb{F}_0$, obtained with the use of the wing's motions (trajectories profiles), done as follows. Using the standard transformation matrix ${}^0R^\mathrm{b}$ for the Z-Y-X Euler transformation convention, which maps vectors written with respect to the body frame $\mathbb{F}_\mathrm{b}$ to the inertial frame $\mathbb{F}_0$, the instantaneous vertical position, Z_c, and vertical acceleration, a_Z, of the wing's center of mass with respect to the inertial frame $\mathbb{F}_0$ can be computed as

$$Z_\mathrm{c} = -\,x_\mathrm{c} + y_\mathrm{c}\cos\theta\sin\psi + z_\mathrm{c}\cos\psi\cos\theta \approx y_\mathrm{c}\psi\cos\theta + z_\mathrm{c}\cos\theta, \tag{21}$$

$$a_Z = y_\mathrm{c}(\ddot{\psi}\cos\theta - 2\dot{\psi}\dot{\theta}\sin\theta) - (y_\mathrm{c}\psi + z_\mathrm{c})(\dot{\theta}^2\cos\theta + \ddot{\theta}\sin\theta) = \; a_{Z_\psi} + a_{Z_\theta}, \tag{22}$$

where $\{x_\mathrm{c}, y_\mathrm{c}, z_\mathrm{c}\}$ are the coordinates of the wing's center of mass with respect to the frame $\mathbb{F}_\mathrm{b}$, where clearly $x_\mathrm{c} \approx 0$. Notice that although there are coupled terms in Eq. (22), a_Z can be divided into two parts, $a_{Z_\psi} = y_\mathrm{c}(\ddot{\psi}\cos\theta - 2\dot{\psi}\dot{\theta}\sin\theta)$ and $a_{Z_\theta} = -(y_\mathrm{c}\psi + z_\mathrm{c})(\dot{\theta}^2\cos\theta + \ddot{\theta}\sin\theta)$, accounting for the contributions from ψ and θ, respectively.

As already mentioned, the experimental rolling angle ψ is significantly smaller than the pitching angle θ and the flapping angle ϕ, but this does not necessarily imply that the inertial force component ma_{Z_ψ} is also significantly smaller than ma_{Z_θ} and that ma_{Z_ψ} can be neglected in the computation of the experimental ma_Z. In fact, the processing of the experimental data shows that the value of ma_{Z_ψ} has a similar magnitude to that of ma_{Z_θ}, as shown in Fig. 6-(a). The explanation for the appearance of this phenomenon is that the experimental signal ψ in Fig. 6-(a) oscillates violently, which implies the existence of high-frequency components with small amplitudes. The difficulty that arises in this situation is that at the same time we would like to eliminate high-frequency noise without filtering out true physical high-frequency information. Empirically, we discovered that both an 8-term *Fourier series* (FS) fitting and the use of a low-pass *zero-phase* (ZP) digital filter with a cutoff frequency of 1 KHz work reasonably well. The instantaneous total vertical force, F_Z computed using the 8-term Fourier series fitting, $F_{Z,\mathrm{FS}}$, is compared to the experimentally measured total vertical force $F_{Z,\mathrm{EXP}}$ in Fig. 6-(b). Similarly, the instantaneous total vertical force, F_Z, computed using the low-pass zero-phase filter, $F_{Z,\mathrm{ZP}}$, is compared to the experimentally measured total vertical force $F_{Z,\mathrm{EXP}}$ in Fig. 6-(c). In the rest of this paper, the respective estimated and filtered inertial forces associated with $F_{Z,\mathrm{FS}}$ and $F_{Z,\mathrm{ZP}}$ are labeled as $ma_{Z_\psi,\mathrm{FS}}$ and $ma_{Z_\psi,\mathrm{ZP}}$. The plot in Fig. 6-(b) shows that $F_{Z,\mathrm{FS}}$ and $F_{Z,\mathrm{EXP}}$ agree reasonably well over the low-frequency range as both signals have fundamental and first harmonic components with approximately the same frequencies and approximately the same phases. From observing Fig. 6-(b), the regions with the most noticeable mismatches are marked as A, B, C and D. In region C, the aerodynamic lift F_L is small, as can be seen in Fig. 5-(a), and the inertial force dominates the resultant force F_Z. Therefore, the discrepancy over this region is most likely due to errors in the computation of the instantaneous inertial force, as the experimental measurement of the rolling angle ψ is not highly reliable, because it has been corrupted with significant sensor and post-processing noise. Evidence supporting this hypothesis can be observed in Fig. 6-(c), where the total vertical force estimated using the zero-phase low-filtered inertial force matches the experimental measurement significantly better over region C, suggesting that high-frequency sensor noise overlaps with high-frequency physical information that might be filtered out with the Fourier-series method, degrading the agreement between $F_{Z,\mathrm{FS}}$ and the $F_{Z,\mathrm{EXP}}$. The same reason might explain the mismatch between $F_{Z,\mathrm{FS}}$ and $F_{Z,\mathrm{EXP}}$ over region A in Fig. 6-(b) and the much better agreement between $F_{Z,\mathrm{ZP}}$ and $F_{Z,\mathrm{EXP}}$ over region A in Fig. 6-(c). Over regions C and D, in both plots, Fig. 6-(b) and Fig. 6-(c), the discrepancies appear as fluctuation patterns of difference in phase and magnitude. The causes for these differences might originate in the measurement and post-processing of the randomly oscillating rolling angle ψ, or might reflect the existence of dissipation or dispersive errors arising in the aerodynamic simulation. It follows that the reliability of the aerodynamic simulation should not be assessed from the comparison of the instantaneous total vertical forces alone, and consequently, more sophisticated experimental validation methods for the simulation results need to be developed in the future.

From the mean value perspective, the measured average vertical force reported in Ref. 15 is 701.7 μN (71.6 mg). In this work, using the aerodynamic lift data from the third and fourth periods of the simulation, the calculated averages of $F_{Z,\mathrm{FS}}$ and $F_{Z,\mathrm{ZP}}$ are $\bar{F}_{Z,\mathrm{FS}} = 715.4\ \mu$N (73.0 mg) and $\bar{F}_{Z,\mathrm{ZP}} = 713.4\ \mu$N (72.8 mg), respectively. Taking into consideration that the most likely sources of disagreement between the experimental and simulated instantaneous total vertical forces are high-frequency small-amplitude measurement and post-processing errors, it is not surprising that the coincidence between the experimental and simulated average vertical forces is high. This is further evidence that, in the cases considered here, aerodynamic simulations are well suited for understanding the dynamics of flapping airfoils and how the forces required for sustained flight are generated, particularly in the normal hovering case. A significant advantage of methods based on CFD for computing aerodynamic forces with respect to quasi-steady blade-element methods is that characteristic geometric wing parameters and force coefficients, typically arduously estimated through wind-tunnel experiments, are not required. Generally speaking, the reasonably *good* match between experimental and simulated vertical forces in the discussed active-pitching case illustrates the effectiveness of the 3-D aerodynamic solver in the estimation of forces acting on the surfaces of flapping wings, and therefore, it is clear that for the considered range of Reynolds number, CFD simulations can be employed in the study of the dynamics of passively-pitching actively-flapping wings. This topic is investigated below in Section III.B.2.

III.B.2. Passive-Pitching Simulation

The simulation discussed in this section is implemented with the same aerodynamic solver configuration and flapping motion profile employed in the active-pitching simulation case, discussed in Section III.B.1. In contrast, the pitching motion, angle θ, is computed dynamically at each simulation step using Eq. (11) and according to the data flow diagram in Fig. 3. In this case, the flexure hinge flexes passively, the reason for which we refer to this numerical implementation as a *passive-pitching* simulation. The parameters relating to the hinge and wing mass distribution used in this simulation are listed in Table 1, where $\phi(0) = -16.17^\circ$ and $\theta(0) = 54.85^\circ$ are the initial conditions used in the simulation, $\Delta t = 0.1$ ms is the simulation step time

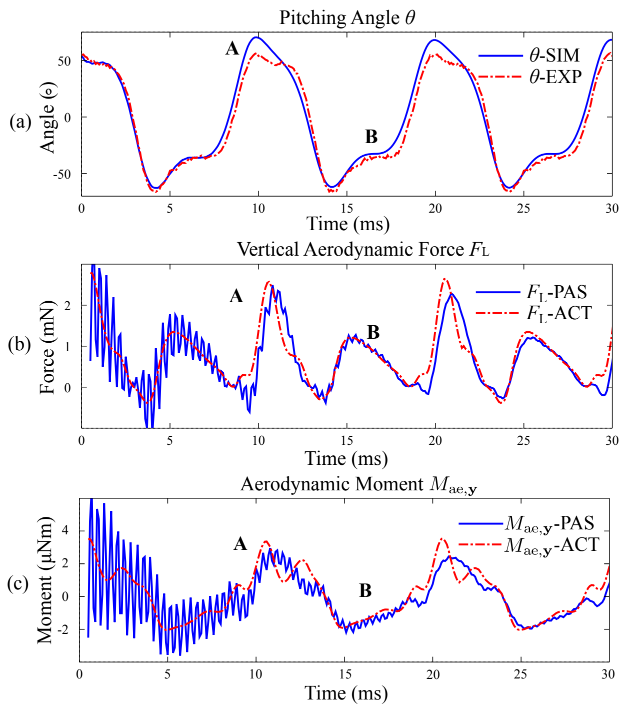

Figure 7. Passive-pitching simulation results. (a) Comparison between the simulated wing-pitching angle, θ-SIM, and the experimentally measured wing-pitching angle in Ref. 15, θ-EXP. **(b)** Comparison between the total aerodynamic force resulting from the passive-pitching simulation, F_L-PAS, and the total aerodynamic force resulting from the active-pitching simulation, F_L-ACT. **(c)** Comparison between the aerodynamic moment $M_{ae,\mathbf{y}}$ resulting from the passive-pitching simulation, $M_{ae,\mathbf{y}}$-PAS, and the aerodynamic moment $M_{ae,\mathbf{y}}$ resulting from the active-pitching simulation, $M_{ae,\mathbf{y}}$-ACT.

Table 1. Parameters Used in the Passive-Pitching Simulations.

$\phi(0)$ (°)	$\theta(0)$ (°)	k_h (μNm $\cdot$ rad^{-1})	Δt (ms)	J_x (mg $\cdot$ mm^2)	J_y (mg $\cdot$ mm^2)	J_z (mg $\cdot$ mm^2)	J_{yz} (mg $\cdot$ mm^2)
-16.17	54.85	2.3520	0.1	43.0	1.7	41.3	-3.5

and the other variables have been already defined. The comparison between the simulated pitching angle, θ-SIM, and the experimentally measured pitching angle θ-EXP, is shown in Fig. 7-(a). In this plot, an excellent agreement between the respective magnitudes and phases is observed, except for the peak marked with an A and the other periodically repeated peaks that follow. The proposed integrated simulation scheme in Fig. 3 is demonstrated to be effective, directly from this benchmark comparison between experiment and simulation.

The instantaneous aerodynamic magnitudes F_L and $M_{ae,\mathbf{y}}$, obtained as results of the active-pitching and passive-pitching simulations are compared in Fig. 7-(b) and Fig. 7-(c), respectively. In contrast to the active-pitching simulation results, the aerodynamic force and moment signals produced by the passive-pitching simulations exhibit significant oscillation over the first two periods. The reason for this behavior is that the initial flow field is not consistent with the initial computed kinematics. In the cases considered in this work, the duration time as well as the magnitude of the overshoots can be reduced significantly by decreasing the size of the simulation time step.Thus, a tradeoff situation emerges in which the duration of the transient can be reduced at the cost of increasing the total simulation time.

The results obtained with the passive-pitching simulation illustrate the effectiveness of the proposed integrated simulation approach in Fig. 3 and also provide strong evidence supporting the reliability of the aerodynamic solver, STAR-CCM+. In the passive-pitching simulation case, since the pitching angle θ is computed by solving Eq. (11), it follows that the evaluation of the relevant aerodynamic variables is reliable and accurate, as long as the predicted pitching angle is also reliable and accurate. This fact is true because the resulting aerodynamic moments can be uniquely determined from given flapping and pitching angles. As can be observed in region B of the plot in Fig. 7-(a), the numerically computed pitching angle, θ-SIM, closely matches the experimentally measured pitching angle, θ-EXP. Also, in Fig. 7-(b) and Fig. 7-(c), it can be seen that the steady-state aerodynamic force F_{L}-PAS and moment $M_{\mathrm{ae},\mathbf{y}}$-PAS obtained from the passively pitching simulation are very similar to the aerodynamic force F_{L}-ACT and moment $M_{\mathrm{ae},\mathbf{y}}$-ACT, obtained as results from the active-pitching simulation, especially in region B. Therefore, the plots in Fig. 7 suggest that, at least in region B, the aerodynamic solver run with the overset grid method is suitable for simulating the dynamics of passively rotating flapping wings of the kind discussed in this paper. Furthermore, it is possible to conclude that since the proposed simulation method in Fig. 3, implemented with the chosen aerodynamic solver (STAR-CCM+), provides a reasonably good estimation of the aerodynamic forces acting on the wing's surfaces. Consequently, it is possible to conclude that the proposed approach can be employed in the future to extract from experimental data accurate estimations of the inertial force component in the total vertical force, experimentally measured as in Ref. 15, already discussed in Section III.B.1.

As mentioned above, a noticeable discrepancy between the numerically predicted and experimentally measured pitching angles can be observed in region A of the plot in Fig. 7-(a). Here, it is clear that the simulated angle has a larger magnitude than that of the experimental angle and also exhibits a slight phase lag near the peak A. Possible explanations for the appearance of these phenomena include aerodynamic simulation errors, unmodeled flexible behavior of the wing and unmodeled nonlinear dynamics of the flexure hinge. In the future, to further quantify aerodynamic simulation errors, direct and indirect experimental measurements of the inertial and aerodynamic forces are required. This approach will overcome the problems associated with the indirect method described in Ref. 15, which calculates aerodynamic forces from total vertical forces and kinematic analyses. Also, as noticeable wing deformations around the region A are reported in Ref. 15, it is clear that a better model of the wing, which in reality is flexible (and not rigid), is also required. We believe that a better flexible model of the airfoil could help eliminate the discrepancy in region A.

Finally, it is important to mention that as argued in Ref. 19, it is reasonable to expect that variations of the flexure hinge stiffness can lead to a phase shift of the wing pitching angle, and therefore, the observed phase difference between the simulated pitching angle, θ-SIM, and the experimental pitching angle, θ-EXP, in Fig. 7-(c) is most likely explained by the unmodeled nonlinear time-varying behavior of the flexure hinge. To see this phenomenon, notice that the absolute value of the experimental rolling angle ψ in Fig. 4-(c) could be as large as 4°, which implies that the flexure hinge deforms inhomogeneously, so that the deformation difference at the extreme of the hinge along the axis $\mathbf{y}$ could take random values as large as $w_{\mathrm{h}}\Delta\psi \approx 125\ \mu$m, which is more than the total length of the hinge, $l_{\mathrm{h}} = 70\ \mu$m. This observed experimental behavior of the hinge is clearly not captured by the stiffness model employed in the simulation, which is assumed to behave as a single-axis simple beam deforming according to a perfectly circular arc form. Clearly, the model used here does not account for multi-axis effects and large deformations, the reason for which its improvement is a matter of current and future research.

In summary, despite minor sporadic short-duration discrepancies between the numerically simulated and the experimentally measured pitching angles, the single-axis beam model for the flexure hinge and the proposed integrated simulation method have been demonstrated to be suitable for the study of the dynamics of flapping wings with passively rotating flexure mechanisms. Notice that even if the presence of discrepancies between experimental and simulation data is due to differences between the true mechanics of the flexure hinge and the simple linear model employed in the simulations, parametric studies of the hinge stiffness can be performed using the integrated simulation scheme in Fig. 3 in order to improve, and eventually optimize, the design of the flexure hinge mechanisms for passive wing rotation.

IV. DISCUSSION

In this section, we demonstrate how the proposed integrated simulation method described in Section III, illustrated by the data-flow diagram in Fig. 3, can be employed to investigate a number of research topics relevant to the understanding of flapping-wing MAVs. Here, we apply the proposed simulation method to address four specific research topics. First, we study the instantaneous location of the center of pressure generated on airfoils as they flap and passively rotate over a flapping cycle. The second topic we study in this section is energy consumption and torque production and their requirements for the operation of passively pitching actively-flapping wing systems built with flexure-hinge-based mechanisms. The third topic investigated in this section is the relationship between flapping-frequency and hinge-stiffness as inputs and wing-pitching angle trajectories as outputs. Finally in this section, we analyze the effect of planform shape on the aerodynamic performance of actively-flapping passively-pitching wings, for a fixed flexure-hinge

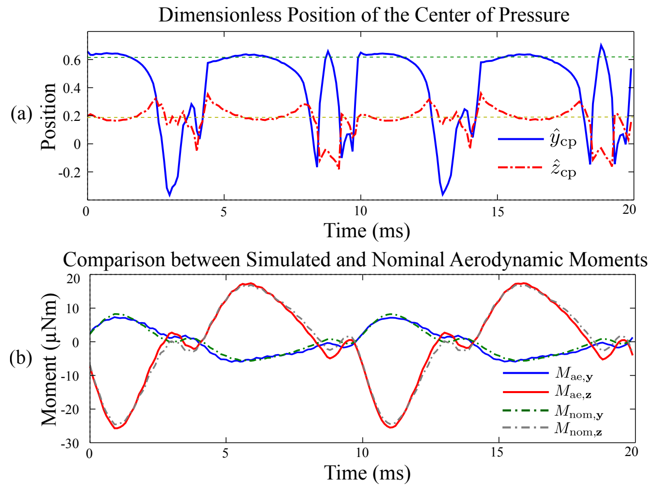

Figure 8. Center of pressure and aerodynamic moments. (a) Instantaneous dimensionless position of the center of pressure on the wing's surface, $\{\hat{y}_{\mathrm{cp}}, \hat{z}_{\mathrm{cp}}\}$, with respect to the body frame $\mathbb{F}_{\mathrm{b}}$. **(b)** Comparison between the magnitudes of the simulated and nominal aerodynamic moments about axes $\mathbf{y}$ and $\mathbf{z}$, respectively.

stiffness.

IV.A. Location of the Center of Pressure

There are many research reasons for why understanding and predicting the generation of aerodynamic force distributions and the location of the associated centers of pressure on the flapping wings of the generic flapping-wing MAV considered in this paper is relevant and useful. For example, when quasi-steady blade-element-based analyses and empirical formulas are employed, the location of the center of pressure on the wing's surface is crucial in the computation of aerodynamic moments using empirical formulas. Thus, since the location of the center of pressure depends on the shape and attitude of the wing, the proposed integrated simulation method can be used to calculate the instantaneous location of the center of pressure for prescribed kinematics (pitching angle θ and flapping angle ϕ), and in this way validate and revise the empirical formulas for specific airfoil designs and mechanism configurations. Here, to compute the location of the center of pressure, we first compute the total pressure force acting on the wing, $\mathbf{F}_{\mathrm{p}}$ and the total pressure moment about the fixed point $\mathbf{O}_{\mathrm{b}}$, $\mathbf{M}_{\mathrm{p}}$, as

$$\mathbf{F}_{\mathrm{p}} = \sum_{i}^{N_{\mathrm{e}}} \mathbf{f}_{\mathrm{pres},i}, \tag{23}$$

$$\mathbf{M}_{\mathrm{p}} = \sum_{i}^{N_{\mathrm{e}}} \left\{ \mathbf{r}_i \times \mathbf{f}_{\mathrm{pres},i} \right\}, \tag{24}$$

where $\mathbf{f}_{\mathrm{pres},i}$ is the normal pressure force acting on the ith surface element of the wing, $\mathbf{r}_i$ marks the position of the ith element from the fixed point $\mathbf{O}_{\mathrm{b}}$ and N_{e} is the total number of elements composing the boundary surface, already defined in Section III.A. Since the wing is rigid and thin, the total pressure force $\mathbf{F}_{\mathrm{p}}$ is normal to the wing plane, and the location of the center of pressure with respect to the body frame $\mathbb{F}_{\mathrm{b}}$ can be computed as

$$\begin{bmatrix} x_{\mathrm{cp}} \\ y_{\mathrm{cp}} \\ z_{\mathrm{cp}} \end{bmatrix} = \begin{bmatrix} 0 \\ -\frac{M_{\mathrm{p},\mathbf{z}}}{F_{\mathrm{p},\mathbf{x}}} \\ \frac{M_{\mathrm{p},\mathbf{y}}}{F_{\mathrm{p},\mathbf{x}}} \end{bmatrix}, \tag{25}$$

where $M_{\mathrm{p},\mathbf{y}}$ and $M_{\mathrm{p},\mathbf{z}}$ are the y and z components of the moment $\mathbf{M}_{\mathrm{p}}$ with respect to the body frame $\mathbb{F}_{\mathrm{b}}$ and $F_{\mathrm{p},\mathbf{x}}$[b] is the x component of $\mathbf{F}_{\mathrm{p}}$ with respect to the body frame $\mathbb{F}_{\mathrm{b}}$. From a practical numerical perspective, the use of Eq. (25) can be problematic, because the magnitude of the normal pressure force $F_{\mathrm{p},\mathbf{x}}$ can become

[b]Notice that in this particular case, $|F_{\mathrm{p},\mathbf{x}}| = \|\mathbf{F}_{\mathrm{p}}\|_2$, because $\mathbf{F}_{\mathrm{p}}$ is perpendicular to the wing's surface.

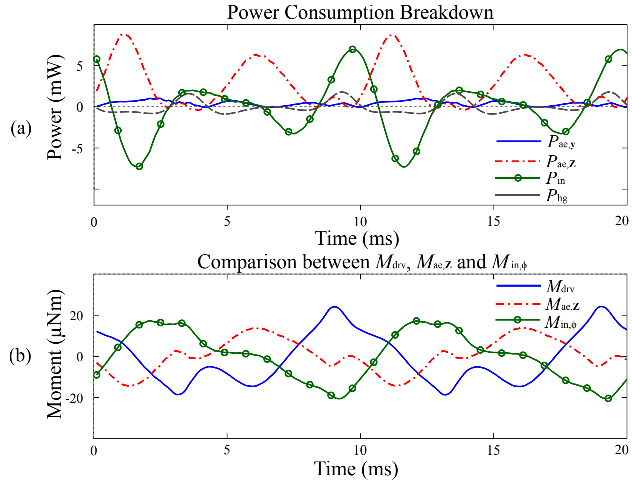

Figure 9. Power consumption and driving moment. (a) Simulated instantaneous power consumption breakdown. **(b)** Comparison between the driving torque, $M_{\rm drv}$, flapping aerodynamic moment, $M_{\rm ae,\mathbf{z}}$, and inertial moment, $M_{\rm in,\phi}$.

very small (close to zero) when either the flapping velocity or pitching angle takes values near zero, creating violent fluctuations and erroneous estimates for $(x_{\rm cp}, y_{\rm cp}, z_{\rm cp})$. To address this numerical issue, a saturation minimum value of 0.5 mN is employed in the estimation of the center of pressure over the wing reversal regions, where the magnitude of the pitching angle θ is very close to zero. The dimensionless coordinates of the center of pressure $\hat{y}_{\rm cp}$ and $\hat{z}_{\rm cp}$ are computed as $\hat{y}_{\rm cp} = y_{\rm cp}R^{-1}$ and $\hat{z}_{\rm cp} = z_{\rm cp}c_{\rm max}^{-1}$, respectively, where R is the spanwise length of the wing and $c_{\rm max}$ is the maximum wing chord. Here, we use $c_{\rm max}$ instead of the standard mean chord $\bar{c}$, because with the use of this definition it is easier to interpret the results and locate by inspection an approximated center of pressure from the dimensionless values $(\hat{x}_{\rm cp}, \hat{y}_{\rm cp}, \hat{z}_{\rm cp})$. In Fig. 8-(a), it can be seen that the center of pressure stays around the average location $(\bar{x}_{\rm cp}, \bar{y}_{\rm cp}, \bar{z}_{\rm cp}) = (0, 0.61R, 0.19c_{\rm max})$ over the non-reversal regions, for the simulation parameters defined in Fig. 4. Notice that if we rearrange Eq. (25) and substitute the mean location of the center of pressure into it, the nominal aerodynamic moment about the $\mathbf{y}$ and $\mathbf{z}$ axes can be obtained as

$$M_{\rm nom,\mathbf{y}} = F_{\rm p,\mathbf{x}}\bar{z}_{\rm cp}, \tag{26}$$

$$M_{\rm nom,\mathbf{z}} = -F_{\rm p,\mathbf{x}}\bar{y}_{\rm cp}. \tag{27}$$

The comparisons between the simulated and nominal aerodynamic moments for the benchmark case are shown in Fig. 8-(b). In this figure, it can be seen that the simulated and nominal signals display a clear good agreement over the non-reversal regions. On the other hand, over the wing reversal region, a noticeable discrepancy in magnitude can be observed. We believe that despite the mismatch over the reversal region, the level of agreement between the nominal and simulated signals is acceptable for quasi-steady analyses, given that the phase matching is almost perfect. Thus, we conclude that the mean location of the center of pressure can be employed to generate a useful empirical expression for the estimation of the total aerodynamic moment, once the magnitude of the normal aerodynamic force $F_{\rm p,\mathbf{x}}$ has been obtained. It is important to mention that the presented results for the estimation of the location of the center of pressure are valid only for the wing shape in Fig. 4-(b), flapping trajectory ϕ in Fig. 4-(c), and the dynamics in Eq. (11) for θ. A more complete and general empirical formula for the estimation of aerodynamic moments, capable of accounting for wing shape variations and diverse flapping and wing-pitching kinematics will be explored through further research.

IV.B. Power, Energy Consumption, and Driving Torque

Insect-scale flapping-wing MAVs of the kind considered here operate under stringent power and energy constraints, and therefore, to achieve full autonomy at the insect-scale, the issues of aerodynamic efficiency and its improvement, and eventually its optimization, are crucial. A first required step in this direction is the development of the capabilities necessary for the reliable estimation of the aerodynamic power and energy associated with fully prescribed kinetics (the flapping trajectory ϕ and the wing-pitching trajectory θ), and specific planform shapes and mechanical characteristics of the wings discussed in this paper.

For a flapping-wing system built with flexure-hinge-based mechanisms, the instantaneous work generated by the corresponding power actuator is converted into four distinct categories of energy. Namely, aerodynamic damping (dissipative energy), kinetic energy of the wing, potential energy of the flexure hinge, and energy dissipated as sound and heat by the flapping mechanism [19,24,30]. Directly from this energy categorization, it follows that the total instantaneous power consumption of the system can be expressed as

$$P_{\mathrm{sys}} = P_{\mathrm{ae}} + P_{\mathrm{in}} + P_{\mathrm{hg}} + P_{\mathrm{diss}}, \tag{28}$$

where P_{ae} is the total aerodynamic power, P_{in} is the total inertial power of the moving wing, P_{hg} is the flexure hinge potential power and P_{diss} is the power dissipated as heat and sound. Since dissipated power through sound and heat is very difficult to model analytically, it makes sense to characterize its contribution to the total amount of power consumption experimentally. Thus, in this case, recognizing its importance, for purely modeling reasons, we consider P_{diss} to be negligible, as also done in Refs. 19, 30. The total aerodynamic power P_{ae} associated with a perfectly rigid flapping-and-pitching wing can be computed directly from the work done by the aerodynamic forces acting on the wing's surfaces, as the wing rotates about the fixed point $\mathbf{O}_{\mathrm{b}}$, with the expression

$$\begin{aligned} P_{\mathrm{ae}} &= -\mathbf{M}_{\mathrm{ae}} \cdot \boldsymbol{\omega} \\ &= -M_{\mathrm{ae},\mathbf{Z}}\dot{\phi} - M_{\mathrm{ae},\mathbf{y}}\dot{\theta} \\ &= P_{\mathrm{ae},\mathbf{Z}} + P_{\mathrm{ae},\mathbf{y}}, \end{aligned} \tag{29}$$

where the angular velocity $\boldsymbol{\omega}$ and aerodynamic moment $\mathbf{M}_{\mathrm{ae}}$ are decomposed along the right-handed frame defined by axis $\mathbf{y}$, axis $\mathbf{Z}$ and the origin $\mathbf{O}_{\mathrm{b}}$. Similarly, the inertial power P_{in} can be calculated directly from the definition of kinetic energy as

$$P_{\mathrm{in}} = \frac{dK}{dt} = \left[\dot{\phi}\ddot{\phi}\sin^2\theta + \frac{1}{2}\dot{\phi}^2\dot{\theta}\sin(2\theta) + \dot{\theta}\ddot{\theta}\right] J_{\mathrm{y}} + \left[\ddot{\phi}\dot{\theta}\cos\theta + \dot{\phi}\left(\ddot{\theta}\cos\theta - \dot{\theta}^2\sin\theta\right)\right] J_{\mathrm{yz}} + \dot{\phi}\ddot{\phi}J_z. \tag{30}$$

Following the same logic, the potential power associated to the flexure hinge P_{hg} is the time rate of change of the potential energy V in the equivalent torsional spring can be written as

$$P_{\mathrm{hg}} = \frac{dV}{dt} = \frac{1}{2}\frac{d(k_{\mathrm{h}}\theta^2)}{dt} = k_{\mathrm{h}}\theta\dot{\theta}. \tag{31}$$

As an example, here we compute and show the components of the power consumption expression in Eq. (28) associated with the passive-pitching simulation for a wing with the geometric parameters in Fig. 4-(b), the prescribed flapping angle ϕ in Fig. 4-(c), a perfectly horizontal stroke plane ($\psi = 0$) and a passively generated wing-pitching θ resulting from the dynamical simulation, graphically described by the data flow diagram in Fig. 3 (benchmark case). The power consumption results for this benchmark case are shown in Fig. 9-(a), which compares the simulated signals of the aerodynamic power components along the $\mathbf{y}$ and $\mathbf{Z}$ axes, $P_{\mathrm{ae},\mathbf{y}}$ and $P_{\mathrm{ae},\mathbf{Z}}$ (in blue and red, respectively), with the total inertial power (in green) and the hinge potential power P_{hg} (in gray). In this example, before the power components are estimated, the calculated aerodynamic moment and kinematic signals are low-pass filtered, employing the same Fourier series fitting described in Section III, to avoid the appearance of oscillations in the estimated power curves. From the data in Fig. 9-(a), by simple inspection, it is possible to conclude that the relative magnitudes of the simulated aerodynamic flapping power $P_{\mathrm{ae},\mathbf{Z}}$, aerodynamic pitching power $P_{\mathrm{ae},\mathbf{y}}$, and inertial power P_{in} are similar in regime (steady-state) to the relative magnitudes of the same variables obtained experimentally, published in Ref. 30. Similarly, assuming a 71.6-mg flapping-wing MAV (similar to the ones in Refs. 1, 9, 10, 11), the simulated power-to-weight ratio is 44.7 $\mathrm{mW} \cdot \mathrm{g}^{-1}$ with an average power of 3.2 mW, which is in the same range of magnitude to that of the experimentally obtained power-to-weight ratios published in Ref. 30. An important feature to notice in Fig. 9-(a) is that the magnitudes of both the flapping aerodynamic power, $P_{\mathrm{ae},\mathbf{Z}}$, and inertial power, P_{in}, are significantly larger than the magnitudes of the wing-pitching aerodynamic power and hinge-bending power. Consequently, despite the fact that the signal P_{in} is relatively large, since the integration of the inertial power over one period is theoretically zero for periodic symmetrical wing rotations, it follows that the aerodynamic damping is the primary cause of energy consumption in the flapping-wing system as a whole.

In the kind of system considered here (shown in Fig. 4), the aerodynamic damping is overcome by the spar torque that drives the wing flapping motion. From simple algebraic manipulations of Eq. (12), the

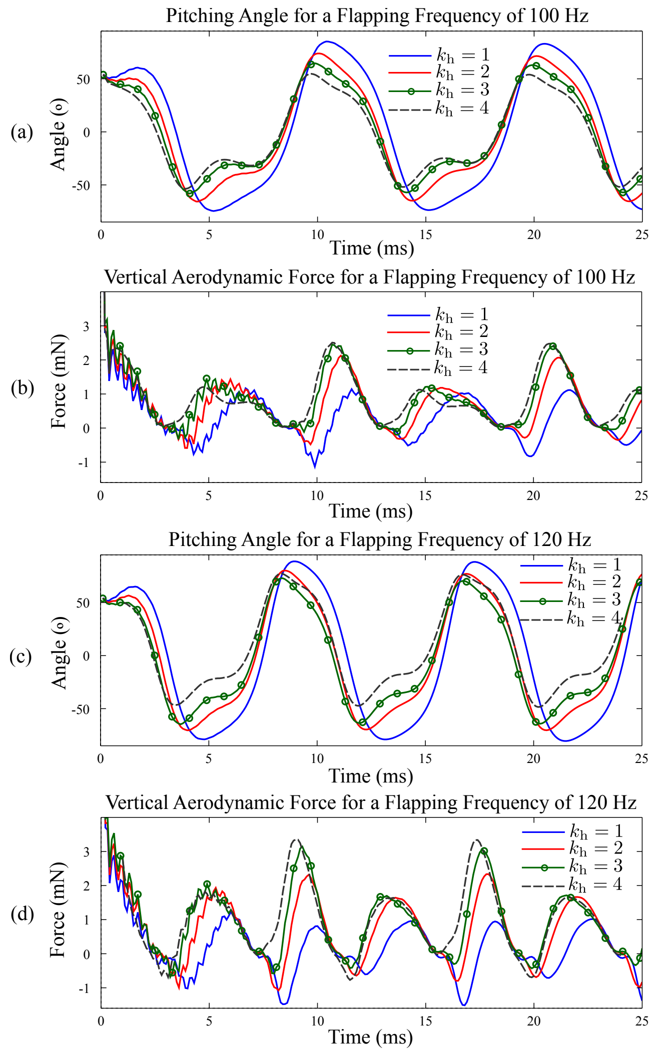

Figure 10. Comparison of the passive-pitching responses for different values of the hinge stiffness coefficient k_h. (a) Simulated wing-pitching angle signals for a flapping frequency of 100 Hz and stiffness coefficient values of 1 μNm $\cdot$ rad^{-1}, 2 μNm $\cdot$ rad^{-1}, 3 μNm $\cdot$ rad^{-1}, 4 μNm $\cdot$ rad^{-1}. **(b)** Simulated total vertical aerodynamic force signals for a flapping frequency of 100 Hz and stiffness coefficient values of 1 μNm $\cdot$ rad^{-1}, 2 μNm $\cdot$ rad^{-1}, 3 μNm $\cdot$ rad^{-1}, 4 μNm $\cdot$ rad^{-1}. **(c)** Simulated wing-pitching angle signals for a flapping frequency of 120 Hz and stiffness coefficient values of 1 μNm $\cdot$ rad^{-1}, 2 μNm $\cdot$ rad^{-1}, 3 μNm $\cdot$ rad^{-1}, 4 μNm $\cdot$ rad^{-1}. **(d)** Simulated total vertical aerodynamic force signals for a flapping frequency of 120 Hz and stiffness coefficient values of 1 μNm $\cdot$ rad^{-1}, 2 μNm $\cdot$ rad^{-1}, 3 μNm $\cdot$ rad^{-1}, 4 μNm $\cdot$ rad^{-1}.

torque $\mathbf{M}_{\mathrm{drv}}$ acting about the wing root can be computed using the prescribed flapping angle ϕ and the simulated pitching angle θ. Given that the driving torque is the only input to the flapping-wing system, the simulated driving torque can serve as the starting point for controller synthesis. Fig. 9-(b) shows the comparison of the simulated driving torque's magnitude, M_{drv}, the aerodynamic moment $M_{\mathrm{ae},\mathbf{Z}}$ and the inertial moment along the ϕ direction, $M_{\mathrm{in},\phi}$. In this figure, it can be clearly observed that the magnitude of the driving torque has the same order of magnitude as the aerodynamic moment magnitude $M_{\mathrm{ae},\mathbf{Z}}$ and inertial moment magnitude along ϕ, $M_{\mathrm{in},\phi}$.

IV.C. Flapping Frequency, Hinge Stiffness, Wing-Pitching Motion, and Force Generation

Through this example we investigate the connections between the value of the flexure-hinge stiffness coefficient, k_h, the resulting wing-pitching motion, θ, and the generation of aerodynamic forces on the wing's surfaces, for two flapping frequencies, in the passive wing-pitching case. We run the simulations employing the method in Fig. 3 for a set of values of the hinge stiffness coefficient ranging from 1 μNm $\cdot$ rad^{-1} to 4 μNm $\cdot$ rad^{-1} with the wing flapping according to prescribed periodic flapping motions with fundamental frequencies of 100 Hz and 120 Hz. The maximum magnitudes and defining parameters of both signals, except

Table 2. Magnitude of the Average Aerodynamic Force, $\bar{F}_{\mathrm{L}}$, for Various Values of the Stiffness Coefficient k_{h} (Single Wing).

k_{h} (μNm $\cdot$ rad^{-1})	$\bar{F}_{\mathrm{L}}$ (μN/mg), 100Hz	$\bar{F}_{\mathrm{L}}$ (μN/mg), 120Hz
1	363.6/37.1	216.6/22.1
2	669.3/68.3	715.4/73.0
3	805.6/82.2	968.2/98.8
4	837.9/85.5	1005.6/102.6

for the frequency, are identical. Thus, the objective behind these simulations is to shed light on the variation of the dynamical behavior of θ, as the flexure-hinge stiffness coefficient, k_{h}, is also varied.

The simulation results illustrating the effect of stiffness-coefficient variation on the dynamic behavior of the pitching θ are summarized in Fig. 10. In Fig. 10-(a) and Fig. 10-(c), it can be observed that as the stiffness coefficient of the hinge is increased from 1 μNm $\cdot$ rad^{-1} to 4 μNm $\cdot$ rad^{-1}, the peaks (local maxima) of the wing-pitching angle signals increase in magnitude, and also these signals display an increasing phase shift to the left. A noticeable difference between the cases in Fig. 10-(a) and Fig. 10-(c) is that, apparently, the phase shift to the left is more significant in the 120-Hz case than in the 100-Hz case. In Fig. 10-(b) and Fig. 10-(d), it can be observed that as the hinge stiffness coefficient is increased from 1 μNm $\cdot$ rad^{-1} to 2 μNm $\cdot$ rad^{-1}, a dramatic increase in the maximum values that the instantaneous total aerodynamic forces signals take. Interestingly, only minor further differences are observed as the hinge stiffness coefficient k_{h} is further increased from 2.0 μNm $\cdot$ rad^{-1} to 3 μNm $\cdot$ rad^{-1} to 4 μNm $\cdot$ rad^{-1}. This behavior might reflect the presence of the phenomenon known as over-rotation, discussed in Ref. 15. If this were to be the case here, over-rotation is explained because a stiffness with a coefficient $k_{\mathrm{h}} = 1$ would be too *soft* in relation to the other parameters of the dynamical system, and consequently, large magnitudes of θ and $\dot{\theta}$ produce effective angles of attack too small to generate significant lift forces. Also in Fig. 10-(b) and Fig. 10-(d), it can be observed that for k_{h} from 2 μNm $\cdot$ rad^{-1} to 4 μNm $\cdot$ rad^{-1}, the amplitudes of the instantaneous lift, F_{L}, are significantly larger for the 120-Hz case than for the 100-Hz case. Similarly, as shown in Table 2, for k_{h} from 2 μNm $\cdot$ rad^{-1} to 4 μNm $\cdot$ rad^{-1}, the average lift also increases noticeably. These simulation results are consistent with the experimental data published in Ref. 7 and with the well-known quasi-steady notion that lift is proportional to the square of the flapping frequency.

Another observation important to make about Figs. 10-(b) and 10-(d) is that, loosely speaking, the instantaneous total vertical force, F_{L}, is *in phase* with the pitching angle θ. This behavior observed in simulation is consistent with the experimental results and analyses in Ref. 18. Finally in this Section IV.C, as can be inferred from Figs. 6-(a) and 6-(b) and Figs. 10-(a) and 10-(b), it is important to note that stiffness coefficients with larger magnitudes ($k_{\mathrm{h}} = 4$ μNm $\cdot$ rad^{-1}, for example) make the simulated and experimental pitching-angle and lift signals match better at the peaks. However, it is clear from the plots that the overall agreement between experimental and simulated signals would be degraded over the non-peak regions if $k_{\mathrm{h}} = 4$ μNm $\cdot$ rad^{-1} were to be used instead of $k_{\mathrm{h}} = 2.3520$ μNm $\cdot$ rad^{-1}. This fact suggests that the stiffness coefficient in reality is time-varying and that it varies from softer to stiffer to softer during a flapping cycle. This hypothesis requires further experimental, numericall and theoretical research in order to be discarded or to remain plausible.

IV.D. Wing Planform Shape

This simulation example studies the relationship between the wing planform shape and the aerodynamic performance achieved by the passively-pitching flapping-wing system, by comparing the aerodynamical behavior of a honeybee-like wing with that of the benchmark wing in Fig. 4-(b), which is biologically inspired by the wings of the species *Eristalis tenax*. For purposes of analysis, we compare wings with the same area and spanwise length, where the honeybee-like wing differentiates from the *Eristalis-tenax*-like wing, because it has a sharper trailing edge. Figs. 11-(a) and 11-(b) show the instantaneous pitching angles and vertical aerodynamic forces resulting from simulations for the two wing planforms considered here, for a flapping frequency of 100 Hz and a flexure-hinge stiffness coefficient of 3 μNm $\cdot$ rad^{-1}. The aerodynamical behavior of the honeybee-like flapping wing exhibits a noticeable phase shift in its pitching angle, when compared to the pitching angle of the benchmark wing (*Eristalis-tenax*-inspired wing). A similar phase shift can be also observed in the vertical aerodynamic force signals. It is clear that the magnitude of the amplitude of

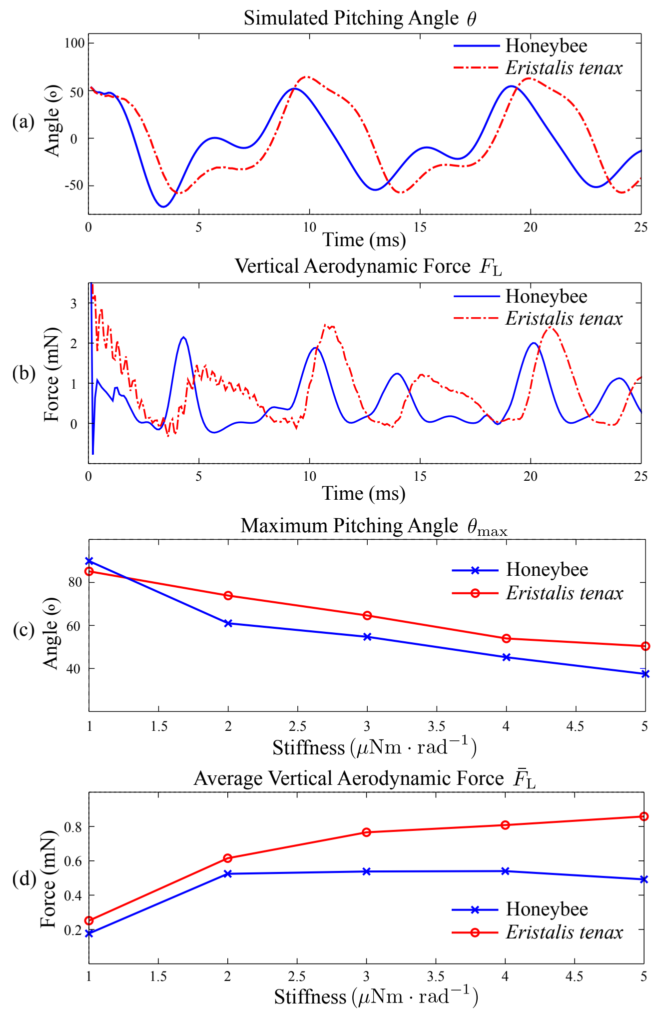

Figure 11. Comparison of passive-pitching simulation results obtained with the models of a perfectly rigid honeybee-like wing and a perfectly rigid *Eristalis-tenax*-like wing. (a) Simulated pitching-angle signals comparing the honeybee-like-wing and *Eristalis-tenax*-like-wing cases, for a stiffness coefficient $k_h = 3\ \mu\text{mN} \cdot \text{rad}^{-1}$. **(b)** Simulated instantaneous total vertical aerodynamic forces corresponding to the honeybee-like-wing and *Eristalis-tenax*-like-wing cases, for a stiffness coefficient $k_h = 3\ \mu\text{mN} \cdot \text{rad}^{-1}$. **(c)** Simulated maximum amplitude of the pitching angle signal, θ_{max}, for five different values of the stiffness coefficient, $k_h = 1\ \mu\text{mN} \cdot \text{rad}^{-1}, 2\ \mu\text{mN} \cdot \text{rad}^{-1}, 3\ \mu\text{mN} \cdot \text{rad}^{-1}, 4\ \mu\text{mN} \cdot \text{rad}^{-1}$ and $5\ \mu\text{mN} \cdot \text{rad}^{-1}$, comparing the honeybee-like-wing and *Eristalis-tenax*-like-wing cases. **(d)** Simulated average total vertical aerodynamic force, $\bar{F}_L$, for five different values of the stiffness coefficient, $k_h = 1\ \mu\text{mN} \cdot \text{rad}^{-1}, 2\ \mu\text{mN} \cdot \text{rad}^{-1}, 3\ \mu\text{mN} \cdot \text{rad}^{-1}, 4\ \mu\text{mN} \cdot \text{rad}^{-1}$ and $5\ \mu\text{mN} \cdot \text{rad}^{-1}$, comparing the honeybee-like-wing and *Eristalis-tenax*-like-wing cases.

the instantaneous total aerodynamic force generated with the *Eristalis-tenax*-like wing is noticeably larger than the one generated with the honeybee-like wing. Similarly, as can be seen in Figs. 11-(c) and 11-(d), the resulting average vertical force, for $k_h = 3\ \mu\text{Nm} \cdot \text{rad}^{-1}$, in the *Eristalis-tenax*-like wing case is significantly larger than the one obtained with the honeybee-like wing.

Figs. 11-(c) and 11-(d), respectively, also show the comparisons of the simulated maximum pitching-angle magnitudes and the average vertical aerodynamic forces for various values of the flexure-hinge stiffness coefficient, ranging from $1\ \mu\text{Nm} \cdot \text{rad}^{-1}$ to $5\ \mu\text{Nm} \cdot \text{rad}^{-1}$. The maximum pitching angles for both wing planforms follow similar patterns. However, the average aerodynamic force generated by the *Eristalis-tenax*-like wing increases monotonically with respect to the value of hinge stiffness coefficient, while the average aerodynamic force generated by the honeybee-like wing follows a unimodal function within the observed stiffness-coefficient range. Finally, the plot in Fig. 11-(d) suggests that, correspondingly, the *Eristalis-tenax*-like wing can achieve even larger average vertical aerodynamic forces by increasing the hinge stiffness coefficient beyond $5\ \mu\text{Nm} \cdot \text{rad}^{-1}$, while the average vertical aerodynamic force generated with the honeybee-like wing seems to have a local maximum (optimal) design point around $3\ \mu\text{Nm} \cdot \text{rad}^{-1}$. The results for these two wing planforms are consistent with the parametric study in Ref. 21. Further parametric studies on the relationship between wing planform and aerodynamic performance can serve as a basis for wing shape and hinge stiffness selection. To finalize this analysis, it is important to mention that the results in Fig. 11 should be interpreted with extreme caution, as the simulations presented here were implemented with the assumption that both simulated wings behave as completely rigid thin objects, which is not true in the case of natural insects' wings.

V. CONCLUSSIONS AND FUTURE RESEARCH

We proposed a new integrated approach for the simulation of the dynamics of an actively-flapping–passively-pitching wing system. In the analysis discussed here, the flexure hinge mechanism employed in the generation of passive wing rotations was modeled as a single-axis flexible beam, using basic solid mechanics theory. The fundamental rigid dynamics equations describing the motions of the actively-flapping and passively-pitching wing were found using the Euler-Lagrange method in Kane's formulation. As usual, the behavior of the air surrounding the flapping wing was modeled employing the 3-D incompressible Navier-Stokes equations, suitable for the insect-scale flapping-wing case, which defines low Reynolds numbers (10^2 to 10^4) and unsteady flows. Mostly satisfactory results for active-pitching and passive-pitching simulation cases were achieved, when compared to experimental results available in the technical literature.

We believe that the obtained simulation results are still preliminary and that further experimental and analytical research is required to validate them. Nonetheless, the proposed approach is significant as it shows a clear path to follow in the analysis, simulation and design of flapping wing systems, which define complex fluid-structure interaction problems. As examples, we showed that the obtained simulation results can be applied to the study of multiple research issues, such as the spatial location of the center of pressure on a flapping airfoil, energy consumption and driving torque requirements of flapping-wing MAVs, specifically in normal hovering flight, or equivalently, in ground tests.

Additionally, we presented a parametric analysis of the flexure hinge stiffness, along with preliminary studies on the effects of different flapping frequencies and wing planform shapes on the generation of aerodynamic forces and moments by the studied flapping-wing system. Once again, the presented results are consistent with the experimental data available in the technical literature, and consequently, we believe that similar approaches can be carried out for the study of other topics, such as inertia distribution and complex flapping kinematics. Therefore, in our view, it is clear that the conjunction of multiple analyses based on the proposed integrated modeling and simulation method can serve as the foundation for advanced microrobotic design of wings, passively-rotating flexure hinge mechanisms and mechanical transmissions in the quest for the development and construction of innovative flapping-wing MAVs.

Considering the obtained simulation results, a research question that still remains unanswered is the cause for the appearance of sporadic short-duration discrepancies between the experimentally measured pitching-angle and the numerically simulated pitching-angle, which could be the result of aggregated aerodynamic simulation errors, unmodeled nonlinear time-varying behavior of the flexure hinge and/or unmodeled wing flexible behavior. Although the most probable explanation for the observed sporadic discrepancies between the experimental and simulated angle θ is the difference between the behavior of the true and modeled flexure hinge, further research is needed to obtain a definitive answer. Once all the discrepancies between experiments and simulations are resolved, the proposed integrated simulation approach could also be employed to investigate issues relating to optimal robotic design and advanced high-performance control. The immediate next step in our research program is the dynamical modeling of an entire insect-scale flapping-wing MAV and its full simulation, employing the same generic integrated approach proposed in this paper. Furthermore, a full dynamical model combined with the 3-D aerodynamic simulation discussed here can be used to study more complex and practical flight situations other than just the perfect normal hovering case or the flapping-wing ground test case.

ACKNOWLEDGMENT

The authors are indebted to Dr. J. P. Whitney for providing the geometric model of the wing and the experimental data used to validate the reported simulation results. This work was supported by the USC Viterbi School of Engineering through a graduate fellowship to L. Chang and a start-up fund to N. O. Pérez-Arancibia.

References

[1] R. J. Wood, "The First Takeoff of a Biologically Inspired At-Scale Robotic Insect," *IEEE Trans. Robot.*, Vol. 24, No. 2, April 2008, pp. 341–347.

[2] J. P. Whitney, P. S. Sreetharan, and R. J. Wood, "Pop-up Book MEMS," *J. Micromech. Microeng.*, Vol. 21, No. 11, Nov. 2011, pp. 115021 (7pp).

[3] P. S. Sreetharan, J. P. Whitney, M. D. Strauss, and R. J. Wood, "Monolithic Fabrication of Millimeter-Scale Machines," *J. Micromech. Microeng.*, Vol. 22, No. 5, May 2012, pp. 055027 (6pp).

[4] N. O. Pérez-Arancibia, J. P. Whitney, and R. J. Wood, "Lift Force Control of a Flapping-Wing Microrobot," *Proc. 2011 Amer. Cont. Conf.*, San Francisco, CA, July 2011, pp. 4761–4768.

[5] N. O. Pérez-Arancibia, J. P. Whitney, and R. J. Wood, "Lift Force Control of Flapping-Wing Microrobots Using Adaptive Feedforward Schemes," *IEEE/ASME Trans. Mechatron.*, Vol. 18, No. 1, Feb. 2013, pp. 155–168.

[6] N. O. Pérez-Arancibia, P. Chirarattananon, B. M. Finio, and R. J. Wood, "Pitch-Angle Feedback Control of a Biologically Inspired Flapping-Wing Microrobot," *Proc. 2011 IEEE Int. Conf. Robot. Biomim.*, Phuket Island, Thailand, Dec. 2011, pp. 1495–1502.

[7] N. O. Pérez-Arancibia, K. Y. Ma, K. C. Galloway, J. D. Greenberg, and R. J. Wood, "First Controlled Vertical Flight of a Biologically Inspired Microrobot," *Bioinspir. Biomim.*, Vol. 6, No. 3, Sept. 2011, pp. 036009–1–11.

[8] Z. E. Teoh, S. B. Fuller, P. Chirarattananon, N. O. Pérez-Arancibia, and R. J. Wood, "A Hovering Flapping-Wing Microrobot with Altitude Control and Passive Upright Stability," *Proc. IEEE/RSJ Int. Conf. Intell. Robot. Syst.*, Vilamoura, Algarve, Portugal, Oct. 2012, pp. 3209–3216.

[9] N. O. Pérez-Arancibia, P.-E. J. Duhamel, K. Y. Ma, and R. J. Wood, "Model-Free Control of a Flapping-Wing Flying Microrobot," *Proc. IEEE Int. Conf. Adv. Robot.*, 2013, pp. 1–8.

[10] K. Y. Ma, P. Chirarattananon, S. B. Fuller, and R. J. Wood, "Controlled Flight of a Biologically Inspired, Insect-Scale Robot," *Science*, Vol. 340, No. 6132, May 2013, pp. 603–607.

[11] N. O. Pérez-Arancibia, P.-E. J. Duhamel, K. Y. Ma, and R. J. Wood, "Model-Free Control of a Hovering Flapping-Wing Microrobot," *J. Intell. Robot. Syst.*, Vol. 77, No. 1, Jan. 2015, pp. 95–111.

[12] C. DiLeo and X. Deng, "Experimental Testbed and Prototype Development for a Dragonfly-Inspired Robot," *Proc. IEEE/RSJ Int. Conf. Intell. Robot. Syst.*, San Diego, CA, Oct. 2007, pp. 1594–1599.

[13] L. Hines, D. Campolo, and M. Sitti, "Liftoff of a Motor-Driven, Flapping-Wing Microaerial Vehicle Capable of Resonance," *IEEE Trans. Robot.*, Vol. 30, No. 1, Feb. 2014, pp. 220–232.

[14] L. Hines, V. Arabagi, and M. Sitti, "Shape Memory Polymer-Based Flexure Stiffness Control in a Miniature Flapping-Wing Robot," *IEEE Trans. Robot.*, Vol. 28, No. 4, Aug. 2012, pp. 987–990.

[15] J. P. Whitney and R. J. Wood, "Aeromechanics of Passive Rotation in Flapping Flight," *J. Fluid Mech.*, Vol. 660, Oct. 2010, pp. 197–220.

[16] Y. Chen, A. L. Desbiens, and R. J. Wood, "A Computational Tool to Improve Flapping Efficiency of Robotic Insects," *Proc. IEEE Int. Conf. Robot. Autom.*, Hong Kong, China, May 2014, pp. 1733–1740.

[17] R. J. Wood, "Design, Fabrication, and Analysis of a 3DOF, 3cm Flapping-Wing MAV," *Proc. IEEE/RSJ Int. Conf. Intell. Robots Syst.*, 2007, pp. 1576–1581.

[18] A. L. Desbiens, Y. Chen, and R. J. Wood, "A Wing Characterization Method for Flapping-Wing Robotic Insects," *Proc. IEEE/RSJ Int. Conf. Intell. Robots Syst.*, 2013, pp. 1367–1373.

[19] G. Lau, Y. W. Chin, J. T. Goh, and R. J. Wood, "Dipteran-Insect-Inspired Thoracic Mechanism with Nonlinear Stiffness to Save Inertial Power of Flapping-Wing Flight," *IEEE Trans. Robot.*, Vol. 30, No. 5, 2014, pp. 1187–1197.

[20] B. Liang and M. Sun, "Nonlinear Flight Dynamics and Stability of Hovering Model Insects," *J. R. Soc. Interface*, Vol. 10, No. 85, 2013, pp. 20130269.

[21] K. Byl, "A Passive Dynamic Approach for Flapping-Wing Micro-Aerial Vehicle Control," *ASME 2010 Dynam. Syst. Contr. Conf.*, 2010, pp. 215–223.

[22] S. P. Sane, "The Aerodynamics of Insect Flight," *J. Exp. Biol.*, Vol. 206, No. 23, 2003, pp. 4191–4208.

[23] H. Liu, "Integrated Modeling of Insect Flight: from Morphology, Kinematics to Aerodynamics," *J. Comput. Phys.*, Vol. 228, No. 2, 2009, pp. 439–459.

[24] M. Sun and J. Tang, "Lift and Power Requirements of Hovering Flight in *Drosophila virilis*," *J. Exp. Biol.*, Vol. 205, No. 16, 2002, pp. 2413–2427.

[25] Z. J. Wang, J. M. Birch, and M. H. Dickinson, "Unsteady Forces and Flows in Low Reynolds Number Hovering Flight: Two-Dimensional Computations vs Robotic Wing Experiments," *J. Exp. Biol.*, Vol. 207, No. 3, 2004, pp. 449–460.

[26] H. Baruh, *Analytical Dynamics*, WCB/McGraw-Hill Boston, 1999.

[27] P. Chirarattananon, N. O. Pérez-Arancibia, and R. J. Wood, "Wing Trajectory Control for Flapping-Wing Microrobots Using Combined Repetitive and Minimum-Variance Adaptive Methods," *Proc. 2012 Amer. Cont. Conf.*, Montreal, Canada, 2012, pp. 3831–3838.

[28] CD-adapco, "STAR-CCM+ Version 9.02 User Guide," 2014.

[29] Y. Lu and G. X. Shen, "Three-Dimensional Flow Structures and Evolution of the Leading-Edge Vortices on a Flapping Wing," *J. Exp. Biol.*, Vol. 211, No. 8, 2008, pp. 1221–1230.

[30] L. Zhao and X. Deng, "Power Distribution in the Hovering Flight of the Hawk Moth *Manduca sexta*," *Bioinspir. Biomim.*, Vol. 4, No. 4, 2009, pp. 046003.